

Star and Cluster Formation in the Sh2-112 Filamentary Cloud Complex

ALIK PANJA,¹ YAN SUN,² WEN PING CHEN,^{3,4} AND SOUMEN MONDAL¹

¹*S. N. Bose National Centre for Basic Sciences, Kolkata 700106, India*

²*Purple Mountain Observatory, Chinese Academy of Sciences, 10 Yuanhua Road, Nanjing 210033, China*

³*Institute of Astronomy, National Central University, 300 Zhongda Road, Zhongli, Taoyuan 32001, Taiwan*

⁴*Department of Physics, National Central University, 300 Zhongda Road, Zhongli, Taoyuan 32001, Taiwan*

(Accepted in ApJ)

ABSTRACT

We present the star formation activity around the emission nebula Sh2-112. At a distance of ~ 2.1 kpc, this H II complex, itself 3 pc in radius, is illuminated by the massive star (O8 V) BD+45 3216. The associated molecular cloud extends in angular scales of $2^{\circ}0 \times 0^{\circ}83$, corresponding to linear sizes of 73 pc by 30 pc, along the Galactic longitude. The high-resolution ($30''$) extinction map reveals a chain of dust clumps aligned with the filament-like structure with an average extinction of $A_V \sim 2.78$ mag, varying up to a maximum of ~ 17 mag. Our analysis led to identification of a rich population (~ 500) of young (average age of ~ 1 Myr) stars, plus a numerous number (~ 350) of H α emitters, spatially correlated with the filamentary clouds. Located near the edge of the cloud, the luminous star BD+45 3216 has created an arc-like pattern as the ionizing radiation encounters the dense gas, forming a blister-shaped morphology. We found three distinct young stellar groups, all coincident with relatively dense parts of the cloud complex, signifying ongoing star formation. Moreover, the cloud filament (excitation temperature ~ 10 K) traced by the CO isotopologues and extending nearly ~ 80 pc is devoid of ionized gas except at the dense cores (excitation temperature ~ 28 – 32 K) wherein significant ionized emission excited by OB stars (dynamical age ~ 0.18 – 1.0 Myr) pertains. The radial velocity is dynamic (median ~ -3.65 km s⁻¹) along the main filament, increasing from Galactic east to west, features mass flow to form the massive stars/clusters at the central hubs.

Keywords: star formation, star forming regions, pre-main sequence stars, H II regions, ionization, interstellar extinction, molecular clouds, stellar feedback, individual objects: Sh2-112.

1. INTRODUCTION

Most and perhaps all stars form in clustered environments within molecular clouds. Internal gravitational dynamics prompts cloud fragmentation, with each fragment then collapsing and leading to the onset of prestellar core formation (André et al. 2016). Alternatively, propagation of the ionizing or explosive shocks from massive stars may compress neighboring clouds, hence triggering the next epoch of star formation (Elmegreen 1998; Deharveng et al. 2005). Molecular clouds exhibit complex geometries, including substructures such as sheets and filaments to elongated networks (Evans &

Lada 1991; Falgarone et al. 1991; Elmegreen 1993; Myers 2009). The turbulence from expanding H II regions near a filamentary molecular cloud can generate sequential waves of star-forming cores along the long axis of the filament on either side of an H II region (Fukuda & Hanawa 2000). As the ionization front passes through the cloud, it sweeps up neutral gas, potentially increasing the star formation rate in a dense shell (Elmegreen & Lada 1977). The young protostars are preferentially aligned along the filamentary axis, bearing the imprint of fragmentation of the parental cloud.

The optically visible H II region Sh2-112 (hereafter S112, $\ell = 83^{\circ}7589$; $b = +03^{\circ}2750$), located at a distance of ~ 2.1 kpc (Blitz et al. 1982) toward the rich region of the Orion arm, is physically associated with one of the most active nebulous systems of Cygnus X. It

luminated by the massive source BD+45 3216 of a spectral type of O8 V (Lahulla 1985), probably a double or multiple system, the region shows a circular morphology. The surrounding ionized region created by the massive star could be the possible outcome of a triggering effect and hence an efficient site for next-generation star formation, given its distinct blister shaped distribution (Israel 1978). The associated gas with the region has long been investigated, e.g., the radial velocity ($V_{\text{CO}} = -4.0 \pm 2.0 \text{ km s}^{-1}$, Blitz et al. 1982), ^{13}CO cloud mass ($1880 M_{\odot}$, Dobashi et al. 1994), $\text{H}\alpha$ and infrared luminosities (Hunter & Massey 1990), radio recombination lines (Garay & Rodriguez 1983), etc. So far, the studies have been focused within a diameter of $15'$, despite the fact that S112 is not an isolated region, as we shall demonstrate in this work, that there exist dust structures spanning $\sim 2^{\circ}$ parallel to the the Galactic plane, with a noticeable filamentary pattern connecting all the sub-structures with S112 near the center. This paper aims to diagnose the global star-forming activity via a comprehensive sample of young stellar population plus detailed characterization of the associated molecular and ionized gases on a larger scale than previously reported in the literature.

The paper is organized as follows. Section 2 summarizes the observations and data reduction techniques, followed by Section 3, which derives the dust distribution in the region, and identifies the young stellar population from optical $\text{H}\alpha$ emitters, disk-bearing young stars, to embedded protostars. Their spatial distribution in relevance to radio emission is presented. Section 4 discusses the interplay and possible feedback of massive stars to nearby molecular and ionized gas. Section 5 presents a large-scale ($\sim 2^{\circ}$) filamentary structure hosting multiple dense clumps, for which we investigate with CO emission lines the molecular gas parameters and kinematics, rendering an overall star formation activity in the cloud complex from parental clouds to protostellar formation. Finally, we present a summary of main results in Section 6.

2. DATA ACQUISITION AND REDUCTION

Diagnosing the star formation history in a young cloud complex is hampered partly by the initial series of events occurring within a relatively short time scale ($\sim 5 \text{ Myr}$). Multi-wavelength observations are necessary to get a comprehensive young stellar sample. For example, optical data allow us to select $\text{H}\alpha$ emitters and massive members, whereas infrared observations can reveal embedded or disk-bearing objects. On the other hand, the distribution of dense gas, out of which stars form, is traced by molecular line emission, whereas the dust is

detected either by their thermal radiation or inferred by the level of extinction of background stars. Gas photoionized by massive stars is disclosed by radio continuum radiation. Our work makes use of a variety of these tools, either collected by our own or with archival data sets, with each of which briefed in the following.

2.1. Observational Data

HCT: Optical slit spectroscopic observations toward S112 were carried out using the Himalaya Faint Object Spectrograph and Camera mounted on the 2 m Himalayan Chandra Telescope (HCT). Grism 7 (380–684 nm) with a resolution of 1330 was chosen to cover the critical spectral features seen in massive stars. After the bias and cosmic ray correction, the 1-d spectra were extracted using the APALL task in the IRAF software. The spectra were wavelength calibrated by using the Fe-Ar arc lamp, and then flux calibrated with standard star (Oke 1990) observations. The data were also corrected for the atmospheric extinction and instrument sensitivity availing the standard star observations.

PMO: The molecular line data for the three CO (^{12}CO , ^{13}CO , and C^{18}O) $J=1-0$ isotopologues are obtained as parts of the Milky Way Imaging Scroll Painting (MWISP) project (Su et al. 2019). This ongoing project with an expected time span of more than ten years (2011–2022) provides large-scale CO maps of the northern Galactic plane ($-10^{\circ} < \ell < +250^{\circ}$ and $|b| \lesssim 5.2^{\circ}$) with a planned sky coverage of $\sim 2600 \text{ deg}^2$. The observations are carried out by a 13.7 m diameter single-dish millimetre-wavelength telescope, located in Delingha, China, and is managed by the Purple Mountain Observatory (PMO). The MWISP survey delivers high-quality mapping with uniform sensitivity and moderate resolution ($\sim 50''$), and features a high spatially dynamic range. A multibeam sideband-separating Superconducting Spectroscopic Array Receiver system with an instantaneous bandwidth of 1 GHz is employed for simultaneous observations. Typical system temperatures are $\sim 250 \text{ K}$ for ^{12}CO at the upper sideband, and $\sim 140 \text{ K}$ for ^{13}CO and C^{18}O at the lower sideband. The observations are made in position-switch On-The-Fly mode with a sampling interval of $10''$ – $15''$. Typical rms noise levels are $\sim 0.5 \text{ K}$ for ^{12}CO at the velocity resolution of 0.16 km s^{-1} , $\sim 0.3 \text{ K}$ for ^{13}CO and C^{18}O at 0.17 km s^{-1} . The noise suppression and signal identification methods are described in detail by Sun et al. (2021). Finally the raw data are resampled with a grid spacing of $30''$ and mosaicked into FITS cubes using the GILDAS (Gildas Team 2013) software.

2.2. Archival Data

Gaia DR2: The Gaia Data Release 2 (Gaia DR2; Gaia Collaboration et al. 2018) contains homogeneous astrometry on five parameters (celestial coordinates, trigonometric parallaxes, and proper motions) for more than 1.3 billion objects, supplemented with photometry of three broad-band magnitudes in G (330–1050 nm), G_{BP} (330–680 nm), and G_{RP} (630–1050 nm) with unprecedented accuracy. We adopted the distances computed by Bailer-Jones et al. (2018), which provides estimated distances using Gaia parallaxes, with a probabilistic inference approach, by taking into account for the nonlinearity of the transformation and the positivity constraint of a distance value. For this work, the Gaia DR2 measurements are found consistent with those in Gaia Early Data Release 3 (Gaia EDR3; Gaia Collaboration et al. 2021). IPHAS: The Isaac Newton Telescope (INT)/Wide Field Camera (WFC) Photometric $H\alpha$ Survey of the Northern Galactic Plane (IPHAS; Drew et al. 2005) is an imaging survey covering an 1800 deg² sky in broadband Sloan r (624 nm), i (774.3 nm), and narrow-band $H\alpha$ (656.8 nm) filters. The WFC generates a mosaic of four CCD images at a pixel scale of $0''.33$ pixel⁻¹, offering the capability to detect $H\alpha$ emission-line candidates by on-off ($H\alpha$ and continuum) photometry.

UKIDSS and 2MASS: The near-infrared J (1.25 μm), H (1.65 μm), and K (2.16 μm) bands photometric data are obtained from the UKIDSS DR10PLUS Galactic Plane Survey (GPS; Lawrence et al. 2007) and the 2MASS Point Source Catalog (PSC; Skrutskie et al. 2006). UKIDSS has a finer angular resolution ($0''.8$ pixels) compared to 2MASS ($2''.0$ pixels), as well as a deeper sensitivity. The reliable UKIDSS sources are accessed using the Structured Query Language (SQL¹) interface (Lucas et al. 2008). To avoid the inferior photometry, UKIDSS brighter ($J < 13.75$ mag, $H < 13.25$ mag, and $K < 12.50$ mag) sources are supplemented with 2MASS (Alexander et al. 2013). For our work the photometric error for each of the three bands is restricted within 0.1 mag as a quality criterion so as to get a signal-to-noise ratio $\gtrsim 10$.

WISE: The Wide-field Infrared Survey Explorer (WISE; Wright et al. 2010) has scanned the entire sky in four wavebands (3.4, 4.6, 12, and 22 μm) with an angular resolution of $6''.1$, $6''.4$, $6''.5$, and $12''.0$, respectively. The 3.4 μm and 12 μm filters encompass prominent polycyclic aromatic hydrocarbon features, whereas the 4.6 μm filter measures the continuum emission from small grains, and the 22 μm filter detects stochastic emission from small grains or the Wien’s tail of ther-

mal emission from large grains (Wright et al. 2010). To ensure good quality photometry, we considered only sources with magnitude uncertainties $\lesssim 0.2$ mag.

AKARI: The AKARI survey (Murakami et al. 2007) covers about 90% of the sky in four far-infrared bands centring at 65, 90, 140, and 160 μm , with spatial resolutions ranging from $1'$ to $1'.5$. The detection limit of the four bands reaches 2.5–16 MJy sr⁻¹ with a relative accuracy $< 20\%$. The AKARI data provide information on the properties of dusty material in the interstellar medium that emits primarily between ~ 50 and 200 μm (Doi et al. 2015).

NVSS: The National Radio Astronomy Observatory (NRAO) Very Large Array (VLA) Sky Survey (NVSS; Condon et al. 1998) covers the northern sky (82% of the celestial sphere) at 1.4 GHz (21 cm) with nearly uniform sensitivity and a $\sim 45''$ (FWHM) angular resolution. The radio continuum (Stokes I) maps are extracted from the NVSS archive for our study to trace the ionized gas.

Planck: The Planck space mission measured the anisotropy of the cosmic microwave background in nine frequency bands covering 30–857 GHz with angular resolutions ranging from $31'$ to $5'$ (Planck Collaboration et al. 2016). With its high sensitivity and wide wavelength coverage, Planck provides all-sky maps of the thermal dust emission and, in particular from cold dust mainly associated with dense regions within molecular clouds, relevant for studies of the early phases of star formation.

3. DUST DISTRIBUTION AND YOUNG STARS

The YSOs in the region are identified and characterized by their infrared colors. The $H\alpha$ stars are recognized by their excessive flux in the $H\alpha$ filter relative to that in the short-red (as continuum) filter. Notwithstanding the possibility of red dwarfs with active chromospheric activity, an $H\alpha$ sample seen against a star-forming region is dominated by PMS stars. The spatial distribution of YSO population at different evolutionary stages is then correlated with the dust distribution, estimated by the level of extinction of background stars, to infer the starbirth sequence, as discussed below.

3.1. The Extinction Map

The dust distribution is traced by the extinction of background starlight. We utilized the combined UKIDSS and 2MASS H - and K -band photometry, and constructed a stellar number density count by defining a spatial grid over the target area (Gutermuth et al. 2005). First, the region of our interest is subdivided into rectilinear grids, each of a size of $30'' \times 30''$. The 20 nearest-neighbor sources from the center of each grid

¹ <http://wsa.roe.ac.uk/sqlcookbook.html>

are selected to calculate the mean and standard deviation of the $(H - K)$ color for each grid, excluding the sources for which the $(H - K)$ values deviate $\gtrsim 3\sigma$ from the mean value (Panja et al. 2021). The mean $(H - K)$ color for each grid is then converted to A_K , using the reddening law $A_K = 1.82 \times [(H - K)_{\text{obs}} - (H - K)_{\text{int}}]$, the difference between the observed and the intrinsic color (Flaherty et al. 2007).

An extinction map thus produced is somewhat limited in angular resolution by the detection of a fair number of background stars. Moreover, the color excess for any particular grid is derived in a statistical manner (Lada et al. 1994). Empirically, after a series of trials, we found a $\sim 30''$ grid size, and ~ 20 nearest neighbor stars to be optimal choices, as a compromise between sensitivity and resolution (Panja et al. 2020).

The average intrinsic color $(H - K)_{\text{int}}$ of the background population is measured to be ~ 0.2 mag, by using a nearby control field with a nominal extinction of $A_V = 1.3$ mag. The resulting extinction map is displayed in Figure 1. The derived extinction values range from $A_V \simeq 1.33$ –17.20 mag, or $A_K \simeq 0.12$ –1.55 mag. The extinction is relatively low for most of the region, with an average of $A_V \sim 2.78$ mag, despite the young (age ~ 1 Myr) nature of the complex and nebulous appearance, plausibly as the consequence of dispersal of parental cloud.

While the extinction is nonuniform over the region, a pattern stands out connecting chains of clumps and extending in the Galactic east-west direction, along which the average extinction varies in the order of $A_V \sim 3.5$ mag. The maximum extinction of $A_V \sim 17.20$ mag is observed around $(\ell, b) = (083^\circ 70, +03^\circ 28)$ within the S112 region, which is located roughly at the center of the pattern. Whereas toward the Galactic east (maximum $A_V \sim 16.48$ mag) or west (maximum $A_V \sim 15.78$ mag), the extinction marginally decreases from the peak value.

Our extinction map with an angular resolution of $30''$ and sensitivity down to $A_V \sim 20$ mag serves to guide the identification of heavily embedded sources such as protostellar objects, as will be discussed in the next section.

3.2. The Young Stellar Population

The infrared color excess is an indicator of the amount of retaining circumstellar dust, therefore the evolutionary status, of a YSO. The level of the infrared excess dictates the location of a YSO in an infrared color-color diagram. Initially, we have adopted the three-phase classification scheme from the Koenig et al. (2012), by using a set of UKIDSS and WISE color criteria. Following which, we have used the UKIDSS data alone to iden-

tify additional young sources having excess in the near-infrared bands. In addition to WISE data (angular resolution $\sim 6''$ – $12''$; Wright et al. 2010), we also make use of the images where applicable taken by the Spitzer Infrared Array Camera (Fazio et al. 2004) which has a higher resolution (pixel scale $\sim 1''.2$ pixel $^{-1}$) but does not cover the whole region of our study.

The infrared sample is “sanitized” by removing possible contaminants. Galaxies with elevated star formation activity exhibiting increased polycyclic aromatic hydrocarbon (PAH) emission may mimic a YSO color. Unresolved broad-line active galactic nuclei (AGNs) possess mid-infrared colors very similar to those of young stars (Gutermuth et al. 2009). These PAH/star-forming galaxies, AGNs, the shock-excited extended sources are winnowed out from the YSO sample using a combination of WISE colors.

Next, we identified YSO candidates by using the WISE and other color criteria (Koenig et al. 2012). Such a diagnostic color-color diagram using $W1$, $W2$, and $W3$, shown in Figure 2(a), immediately resulted in 55 Class I and 83 Class II objects. To affirm the near-infrared sample, we added the UKIDSS photometry in addition to WISE 3.4, and 4.6 μm data for heavily embedded protostellar candidates. This method requires dereddening of an object by removing the extinction of the nearest grid in the extinction map discussed in the previous section. Additional eight Class I and 39 Class II objects were rectified with this analysis; the dereddened color-color diagram of this added set of YSOs is shown in Figure 2(b).

The analysis discussed thus far does not include those sources visible in near-infrared, but lacking reliable detection in 12 or 22 μm due to the reduced instrument sensitivity and the bright background emission present at these longer wavelengths. The final scrutiny therefore utilized the WISE 3.4, 4.6, and 22 μm bands to select evolved transition-disk sources, i.e., those with little excess between 3.4 and 12 μm , but being bright at 22 μm , presented in Figure 2(c).

The three-pronged analysis scheme outlined above must be self-consistent; namely a YSO that has been classified as a candidate by one scheme would still be reaffirmed with the others. For example if an object mimicking a Class I behavior in the near-infrared turns out not to have a rising spectral energy distribution at 22 μm , it would be reclassified as a reddened Class II. Likewise, a Class II object with unusually blue colors (Koenig et al. 2012) would be placed back to the unclassified sample. At the end, with a combination of all three analysis schemes, a total of 63 Class I, 122

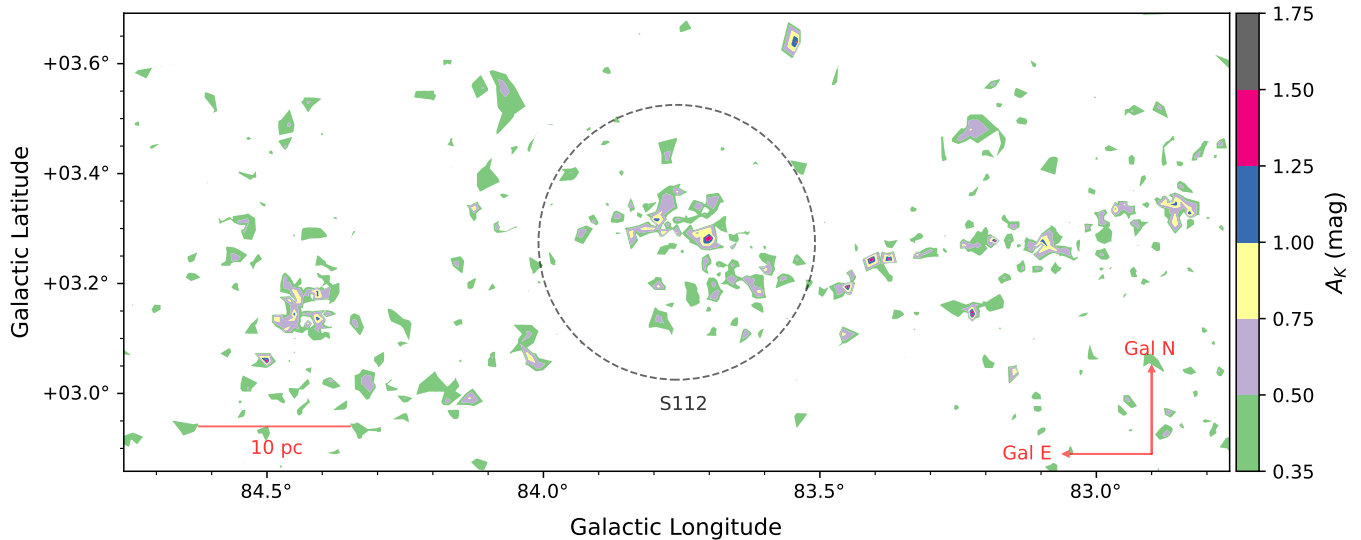


Figure 1. The extinction map around S112 computed by the H - and K -band photometry with a grid size of $30'' \times 30''$. The dashed circle marks the $15'$ radius around S112. Enhanced extinction is seen generally in a zone in the Galactic east-west direction, with a multitude of dense clumps where extinction exceeds $A_K \sim 1.55$ mag, or $A_V \gtrsim 17$ mag. A 10 pc linear scale is displayed assuming a heliocentric distance of 2.1 kpc to the complex.

Class II, and 13 transition-disk objects are identified, whose color-color plot is presented in Figure 2(c).

Furthermore, we have used the UKIDSS colors (Figure 2(d)) to diagnose young objects with excess near-infrared emission, but lacking higher wavelength detection in the previous scheme. The detail methodology is prescribed in Ojha et al. (2011), Panja et al. (2020), and references therein. We have set an additional $(J - H)$ color cut of 1.4 mag in order to remove any possible effects of contamination, based on the analysis of a nearby control field ($\ell = 083^\circ 1441$; $b = +04^\circ 2823$). However, we note that below this limit there would still be a significant number of disk-bearing young sources, but are not included to keep our YSO sample credible. Hereafter, from this method, we found 92 Class I and 252 Class II sources, whereas 41 of them were already detected in

any of the above phases. In case a source is selected with multiple methods, priority is given to WISE colors, because the higher wavelength data provide more robust information about the disk and envelope properties. Thus, finally combining all the methods, we have detected a total of 135 Class I, 353 Class II, and 13 transition-disk objects and their distribution is shown in Figure 2(d). Then again, any of these numbers should be considered as a conservative lower limit, as there are sources detected only in the H and K bands, or only in the K band, but not in the J band. These young stars are listed in Table 1, including relevant infrared photometry, and Gaia data when available; only about 12% of the sources in the table have Gaia DR2 parallax measurements.

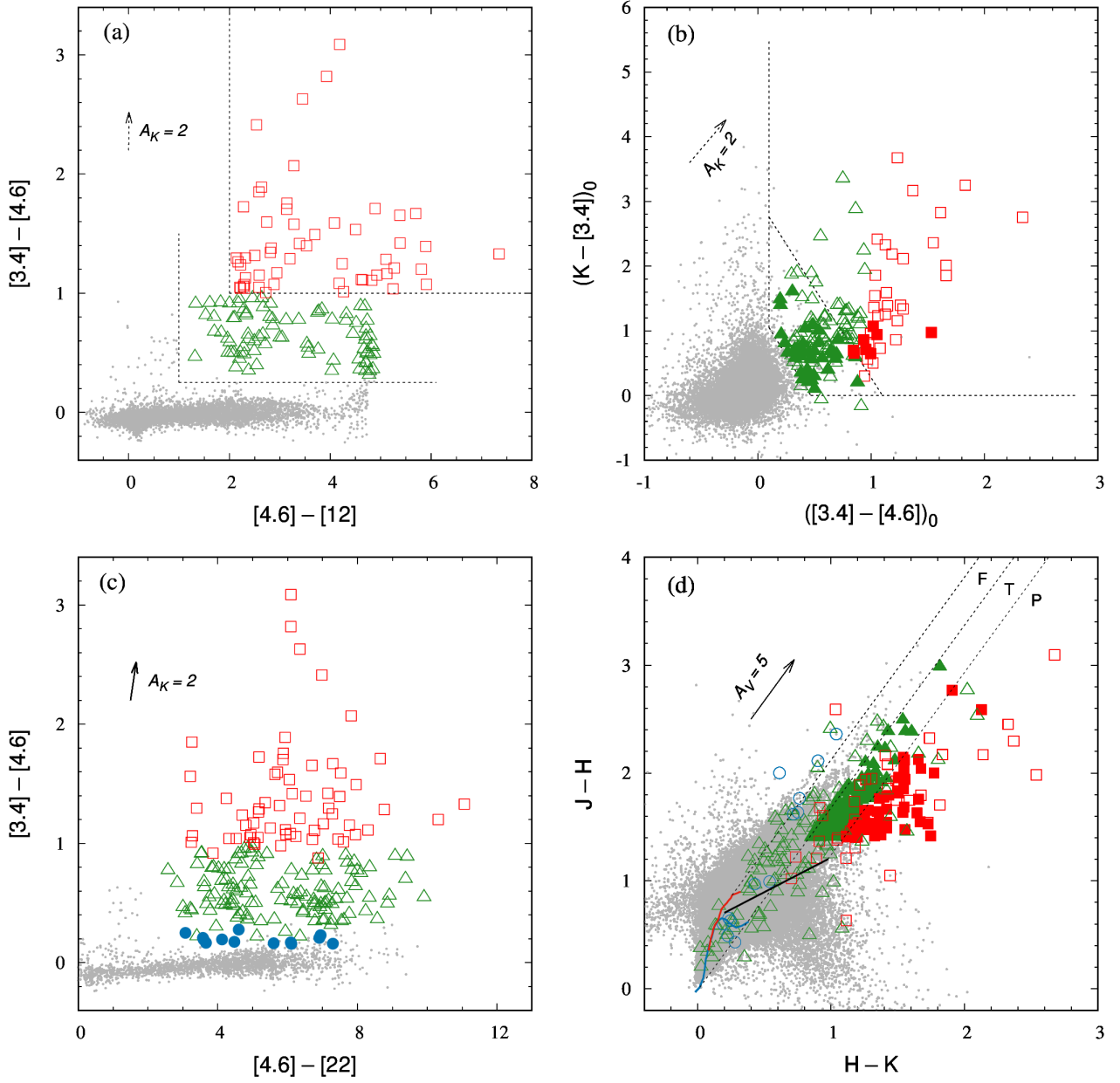


Figure 2. Color-color diagrams of Class I (red squares), Class II (green triangles), transition-disk (blue circles), and non-excess (gray dots) sources, identified by complementary classification schemes (Koenig et al. 2012). In each scheme, the dotted lines denote the adopted color criteria. (a) Class I and Class II objects are selected by the WISE 3.4, 4.6, and 12 μm colors. (b) Heavily embedded sources are recognized by a combination of WISE 3.4 and 4.6 μm , and UKIDSS data. Sources are dereddened in this analysis. Sources that are already found in the previous scheme are shown in open symbols, whereas the additional candidates selected in this scheme are in solid symbols, and a similar sequence is followed for the consecutive plots. (c) This WISE color-color diagram plots all the YSOs identified consistently with three analysis schemes, including the transition-disk objects recognized by WISE 3.4, 4.6, and 22 μm data. (d) Distribution of all the YSOs identified in the previous schemes along with the additional Class I and Class II sources identified only using the excess emission in the UKIDSS bands. The solid blue and red lines mark the locus of dwarfs and giants, both taken from Bessell & Brett (1988), and the solid black line indicates the CTTs locus, taken from Meyer et al. (1997). The three parallel dashed lines represent the reddening vectors. All the photometric data points in this figure are converted to CIT (Elias et al. 1982) system.

Table 1. Photometric catalog of the YSOs toward S112. The table is available in its entirety in machine-readable form

Sl. No.	Glcn. (deg)	Glrat. (deg)	[3-4] μ m (mag)	[4.6] μ m (mag)	[12] μ m (mag)	[22] μ m (mag)	J (mag)	H (mag)	K (mag)	G (mag)	G _{BP} (mag)	G _{RP} (mag)	Distance (kpc)
Class I													
1	83.403456	3.244317	12.307 \pm 0.031	11.043 \pm 0.022	8.872 \pm 0.033	5.878 \pm 0.041	17.522 \pm 0.020	15.682 \pm 0.007	14.125 \pm 0.005
2	83.395593	3.142038	16.110 \pm 0.112	15.036 \pm 0.125	9.128 \pm 0.056	7.093 \pm 0.120
3	83.363773	3.247085	14.877 \pm 0.074	12.807 \pm 0.031	9.529 \pm 0.058	4.985 \pm 0.029
4	83.612797	3.186152	11.288 \pm 0.023	9.946 \pm 0.019	7.136 \pm 0.019	4.589 \pm 0.026	15.410 \pm 0.056	13.982 \pm 0.043	13.018 \pm 0.035	18.828 \pm 0.014	20.130 \pm 0.082	17.300 \pm 0.032	2.375 $^{+1.54}_{-0.77}$
5	83.330033	3.268075	13.229 \pm 0.031	12.219 \pm 0.026	12.307 \pm ...	8.982 \pm ...	18.446 \pm ...	16.154 \pm ...	13.930 \pm 0.057
6	83.360964	2.990175	9.620 \pm 0.022	8.468 \pm 0.021	3.544 \pm 0.015	0.698 \pm 0.005	14.651 \pm 0.057	13.565 \pm 0.061	12.056 \pm 0.031
7	83.457345	3.188119	10.501 \pm 0.024	8.922 \pm 0.019	5.642 \pm 0.015	3.287 \pm 0.019	16.406 \pm 0.008	14.789 \pm 0.004	12.988 \pm 0.002	19.767 \pm 0.018	21.021 \pm 0.158	18.263 \pm 0.048	2.203 $^{+1.98}_{-1.00}$
8	83.251595	3.255542	13.163 \pm 0.029	12.099 \pm 0.024	12.126 \pm ...	8.822 \pm 0.372	17.739 \pm ...	15.708 \pm 0.152	14.152 \pm 0.063
9	83.135417	3.271612	13.042 \pm 0.031	12.164 \pm 0.028	9.833 \pm 0.211	5.287 \pm 0.042	16.859 \pm 0.012	15.033 \pm 0.004	13.798 \pm 0.004
10	83.135074	3.278172	13.408 \pm 0.031	12.373 \pm 0.027	10.353 \pm ...	5.663 \pm 0.056	18.140 \pm 0.036	16.119 \pm 0.011	14.547 \pm 0.007
Class II													
1	83.131848	3.232247	13.443 \pm 0.040	12.669 \pm 0.041	9.545 \pm 0.194	5.951 \pm 0.065	16.601 \pm 0.010	15.451 \pm 0.006	14.611 \pm 0.007	20.039 \pm 0.012	21.347 \pm 0.230	18.737 \pm 0.044	2.379 $^{+2.04}_{-1.11}$
2	83.068837	3.268861	10.922 \pm 0.025	10.422 \pm 0.021	8.455 \pm 0.063	3.659 \pm 0.035	13.667 \pm 0.025	12.675 \pm 0.026	11.864 \pm 0.024	17.003 \pm 0.002	18.281 \pm 0.011	15.779 \pm 0.005	2.457 $^{+0.72}_{-0.47}$
3	83.327383	3.278623	13.418 \pm 0.029	12.983 \pm 0.031	11.613 \pm ...	9.203 \pm ...	16.418 \pm ...	15.215 \pm 0.093	14.364 \pm 0.076
4	83.001149	3.390222	14.675 \pm 0.035	14.181 \pm 0.046	9.462 \pm 0.052	7.909 \pm 0.160	16.601 \pm 0.009	15.674 \pm 0.007	15.245 \pm 0.012	20.728 \pm 0.013	21.369 \pm 0.291	19.230 \pm 0.055	2.239 $^{+2.14}_{-1.30}$
5	83.323391	3.250221	12.478 \pm 0.026	11.703 \pm 0.022	11.325 \pm ...	9.131 \pm ...	18.297 \pm ...	15.615 \pm 0.137	13.437 \pm 0.039
6	83.057411	3.271772	11.963 \pm 0.026	11.436 \pm 0.023	7.677 \pm 0.023	4.689 \pm 0.048	15.236 \pm 0.056	13.938 \pm 0.052	12.891 \pm 0.033	19.469 \pm 0.007	20.630 \pm 0.207	18.044 \pm 0.019	2.691 $^{+2.08}_{-1.19}$
7	83.107832	3.285580	9.800 \pm 0.021	8.984 \pm 0.020	7.457 \pm 0.024	1.995 \pm 0.012	14.068 \pm 0.032	12.206 \pm 0.024	10.964 \pm 0.018	19.512 \pm 0.008	20.885 \pm 0.528	17.819 \pm 0.029	2.530 $^{+2.02}_{-1.11}$
8	83.324920	3.137974	13.559 \pm 0.028	12.906 \pm 0.030	10.537 \pm 0.089	8.468 \pm 0.324	16.116 \pm 0.098	14.843 \pm 0.069	14.426 \pm 0.080	19.535 \pm 0.016	20.510 \pm 0.103	18.263 \pm 0.041	1.700 $^{+1.76}_{-0.83}$
9	83.325522	3.131974	11.872 \pm 0.024	11.374 \pm 0.021	9.287 \pm 0.052	6.974 \pm 0.075	14.320 \pm 0.028	13.273 \pm 0.027	12.652 \pm 0.023	17.538 \pm 0.005	18.682 \pm 0.043	16.398 \pm 0.013	2.601 $^{+0.55}_{-0.55}$
10	83.284975	3.249319	10.168 \pm 0.024	9.541 \pm 0.019	6.542 \pm 0.015	4.878 \pm 0.031	13.555 \pm 0.061	12.399 \pm 0.051	11.518 \pm 0.034	16.892 \pm 0.002	18.171 \pm 0.020	15.708 \pm 0.007	2.289 $^{+0.56}_{-0.38}$
Transition Disk													
1	83.281329	3.251314	11.473 \pm 0.023	11.299 \pm 0.022	9.117 \pm 0.047	6.826 \pm 0.083	15.017 \pm 0.054	13.159 \pm 0.053	12.348 \pm 0.032	20.787 \pm 0.011	21.095 \pm 0.240	18.839 \pm 0.043	1.296 $^{+2.17}_{-0.90}$
2	83.216944	3.055202	12.743 \pm 0.028	12.466 \pm 0.030	10.450 \pm 0.108	7.866 \pm 0.193	14.936 \pm 0.045	13.935 \pm 0.041	13.468 \pm 0.043	17.722 \pm 0.006	18.719 \pm 0.035	16.633 \pm 0.016	2.218 $^{+0.87}_{-0.51}$
3	83.214491	3.055450	11.249 \pm 0.022	11.083 \pm 0.022	9.902 \pm 0.072	7.421 \pm 0.126	12.532 \pm 0.023	11.897 \pm 0.024	11.618 \pm 0.022	14.844 \pm 0.002	15.656 \pm 0.007	13.920 \pm 0.010	3.540 $^{+0.40}_{-0.33}$
4	83.094967	3.295275	12.438 \pm 0.030	12.208 \pm 0.029	10.077 \pm 0.116	5.262 \pm 0.083	14.033 \pm 0.032	13.371 \pm 0.037	13.106 \pm 0.031	16.724 \pm 0.001	17.819 \pm 0.019	15.650 \pm 0.006	2.002 $^{+0.41}_{-0.23}$
5	83.087081	3.238889	12.171 \pm 0.032	12.012 \pm 0.029	9.819 \pm 0.109	4.717 \pm 0.032	15.637 \pm 0.064	13.526 \pm 0.041	12.869 \pm 0.030
6	83.083953	3.286479	9.087 \pm 0.023	8.880 \pm 0.021	6.689 \pm 0.027	1.971 \pm 0.026	13.717 \pm 0.038	11.218 \pm 0.030	10.124 \pm 0.041
7	82.923383	3.154172	11.477 \pm 0.023	11.285 \pm 0.023	9.932 \pm 0.063	7.688 \pm 0.165	13.263 \pm 0.030	12.237 \pm 0.034	11.656 \pm 0.027	17.475 \pm 0.003	19.631 \pm 0.052	16.034 \pm 0.014	3.704 $^{+1.58}_{-0.96}$
8	83.735402	3.161190	12.275 \pm 0.028	12.117 \pm 0.028	10.436 \pm 0.147	6.011 \pm 0.066	15.131 \pm 0.048	13.431 \pm 0.030	12.667 \pm 0.023	20.826 \pm 0.011	21.409 \pm 0.235	19.119 \pm 0.060	1.996 $^{+2.09}_{-1.17}$
9	83.818145	3.134543	11.068 \pm 0.023	10.861 \pm 0.020	9.394 \pm 0.051	7.287 \pm 0.126	14.068 \pm 0.025	12.351 \pm 0.026	11.552 \pm 0.021	19.622 \pm 0.005	21.154 \pm 0.215	17.906 \pm 0.023	2.415 $^{+1.03}_{-0.70}$
10	83.968444	3.647253	11.612 \pm 0.024	11.363 \pm 0.022	10.491 \pm 0.107	8.291 \pm 0.182	12.440 \pm 0.021	12.018 \pm 0.026	11.703 \pm 0.021	14.758 \pm 0.000	15.577 \pm 0.003	13.841 \pm 0.002	2.751 $^{+0.23}_{-0.20}$

3.3. The $H\alpha$ Emitters

Many young low-mass stars show $H\alpha$ in emission, from either chromospheric activity or circumstellar accretion. The IPHAS survey avails the detection of $H\alpha$ emission-line stars, reaching a 10σ sensitivity down to $r \simeq 20$ mag. Figure 3 shows the distribution of sources detected in IPHAS imaging, by considering a reliability criteria of $r < 20$ mag and photometric uncertainty < 0.1 mag in all three bands. The benefit of forming $(r-i)$ as abscissa and $(r-H\alpha)$ as ordinate in the color-color plot is that objects with $H\alpha$ -band excesses appear higher within the diagram, while intrinsically redder or more highly reddened objects are over to the right (Drew et al. 2005), and because the $(r-H\alpha)$ color tends to act as a coarse proxy for the spectral type and is less sensitive to the reddening than $(r-i)$. A star is considered as a $H\alpha$ star if it is located above the track of unreddened main-sequence stars (1) with $H\alpha$ emission strengths more than equivalent width of -10 \AA (Barentsen et al. 2014), and (2) its $(r-H\alpha)$ color is deviated from the main locus of non-emission-line objects by more than three times the average uncertainty of its $(r-H\alpha)$ value.

With this, we found a total of 357 $H\alpha$ emitters toward the S112 region. In Figure 3, a large number of sources have excessive $(r-H\alpha)$ color, reflecting strong $H\alpha$ line strength, while a few of the sources are located toward the higher reddening zone. In contrast, the field star distribution shows two well-defined loci, revealing two distinct stellar populations, one for the unreddened main-sequence and other for the giant stars. An estimation of the reddening from such a color-color diagram would be inappropriate, as the reddening tracks are curved in a way that depends on the spectral energy distribution and the amount of reddening. Among the 357 $H\alpha$ emitters, 14 are found to have infrared counterparts and are previously (Section 3.2) classified as either Class I, Class II, or transition-disk objects. The photometric parameters of the $H\alpha$ emitting sources are detailed in Table 2. More than 97% of the $H\alpha$ emitters have Gaia DR2 parallax measurements.

3.4. Average Age of the YSOs

The average age of the stellar sources, which are the most profoundly traceable entity of a cluster, hints on the timescale and dynamics of the cluster evolution. We have estimated the ages of the YSOs by comparing their (Class I, Class II, and transition-disk) $G_{BP} - G_{RP}$ color vs G magnitude with theoretical isochrones, presented in Figure 4. With the Gaia sensitivity of $G \sim 20$ mag, plus generally a low extinction across the region, Gaia

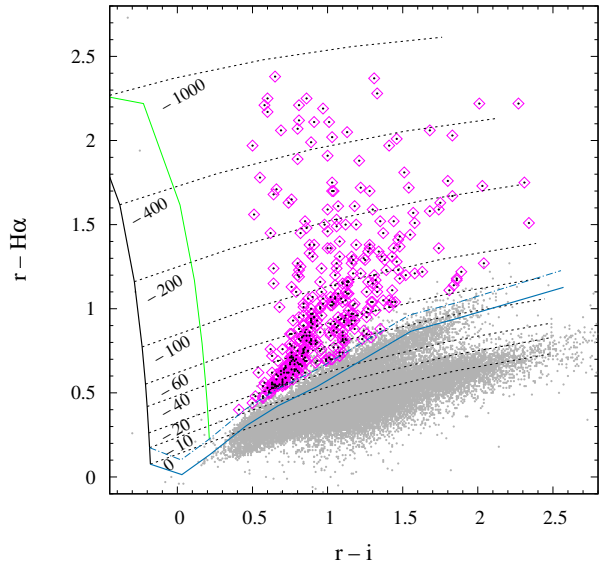


Figure 3. The IPHAS $r-H\alpha$ versus $r-i$ color-color diagram to select $H\alpha$ emission stars. Candidate $H\alpha$ emitters are represented by magenta diamonds, whereas the rest field interlopers are depicted as gray dots. The solid and dashed blue lines represent the unreddened main sequence, which normally serves as the upper bound to the main stellar locus, and the expected position of unreddened main-sequence stars with $H\alpha$ emission strengths of an equivalent width of -10 \AA . The nearly vertical solid black and green lines show the trend for an unreddened Rayleigh-Jeans continuum and the unreddened continuum of an F0 spectral type, respectively. The black broken lines are the predicted lines of constant net emission.

data afford the detection of a handful of YSOs with reliable parallax and proper motion. Going even fainter ($G \gtrsim 20.5$ mag) limit, the detection of lower-mass ($M \lesssim 0.4 M_{\odot}$) membership becomes unreliable. The objects in different subregions are denoted separately to check if they are attributed to any specific age range, but we did not find any systematic trend in the age distribution for different clusters. We deliberately excluded the $H\alpha$ emitters in the age determination because other than being pre-main-sequence objects this sample could incorporate post-main-sequence stars, interacting binaries, supergiants, luminous blue variables, or post-asymptotic giant branch stars among others (Drew et al. 2005). The exclusion of $H\alpha$ stars also applies to distance analysis, to avoid foreground or background contamination.

The stellar evolutionary tracks are taken from the PAdova and TRieste Stellar Evolution Code (PARSEC; Bressan et al. 2012) interactive tool with version release 1.2S. For Gaia sources, we adopted the photometric sensitivity of Evans et al. (2018), as they give empirically the best fit to our data. In the fit of isochrones to the

Table 2. Photometric catalog of the H α emitters toward S112. The entire catalog is available in the electronic version

No.	Glou.	Glat.	r	i	H α	Distance	YSO Class
	(deg)	(deg)	(mag)	(mag)	(mag)	(kpc)	
1	83.325522	3.131974	17.44 ± 0.01	16.33 ± 0.01	16.64 ± 0.01	$2.601^{+0.89}_{-0.55}$	II
2	83.216944	3.055202	17.92 ± 0.02	16.87 ± 0.01	16.86 ± 0.01	$2.218^{+0.87}_{-0.51}$	TD
3	83.131848	3.232247	19.60 ± 0.05	18.41 ± 0.03	18.10 ± 0.03	$2.379^{+2.04}_{-1.11}$	II
4	83.771466	3.278478	18.34 ± 0.01	17.31 ± 0.02	16.59 ± 0.01	$3.316^{+1.59}_{-0.92}$	II
5	83.767700	3.295630	18.04 ± 0.01	16.97 ± 0.01	16.43 ± 0.01	$2.109^{+0.88}_{-0.50}$	II
6	83.799645	3.291358	13.66 ± 0.00	13.02 ± 0.00	12.51 ± 0.00	...	II
7	83.759443	3.319530	19.92 ± 0.04	18.38 ± 0.04	18.20 ± 0.03	$1.409^{+1.62}_{-0.56}$	II
8	83.680314	3.232444	19.82 ± 0.04	18.52 ± 0.04	18.78 ± 0.04	...	II
9	83.612797	3.186152	19.51 ± 0.03	17.88 ± 0.03	18.29 ± 0.03	$2.375^{+1.54}_{-0.77}$	I
10	83.968444	3.647253	14.72 ± 0.00	13.86 ± 0.00	14.03 ± 0.00	$2.751^{+0.23}_{-0.20}$	TD

data, displayed as Figure 4, while there is a spread in the inferred age, the majority of the YSOs are scattered between 0.1–10 Myr, except for a few older than 10 Myr near the zero-age main sequence. The reason for the spread, other than the uncertainties in the isochrones at very young ages, could likely arise from variable (interstellar and circumstellar) extinction of individual sources. A compromising age of the YSO population therefore is ~ 1 Myr.

3.5. Spatial Distribution of the PMS Population

The spatial distribution of the young population reveals essential information regarding the length- and time-scale of the star formation activity in association with a cloud complex. Figure 5 manifests the distribution of Class I, Class II, and transition-disk objects, superimposed on the Planck 353 GHz map, in which existence of a filamentary-like pattern aligned from the Galactic east to west is evident. The location of three high intensity subregions (Clump A, S112, and Clump B) is revealed, with all of them being interconnected via the filamentary structure. Not only the positions of the YSOs are traced along the higher intensity clouds, but also the YSO clustering nicely coincides with the subregions. Moreover, a good degree of similarity is observed between this spatial map with that of the extinction map (Figure 1) derived from the infrared star counts (Section 3.1). Altogether, a combination of spatial distribution of young objects, intensity morphology, and extinction map favours of an ongoing star formation activity in a broader and continuous scale ($\sim 2^\circ$) spanned across the Galactic longitude.

The intensity map unveils fluctuation in the cloud density over the region, with the peak near the S112 subregion, where an elevated concentration of YSOs is also

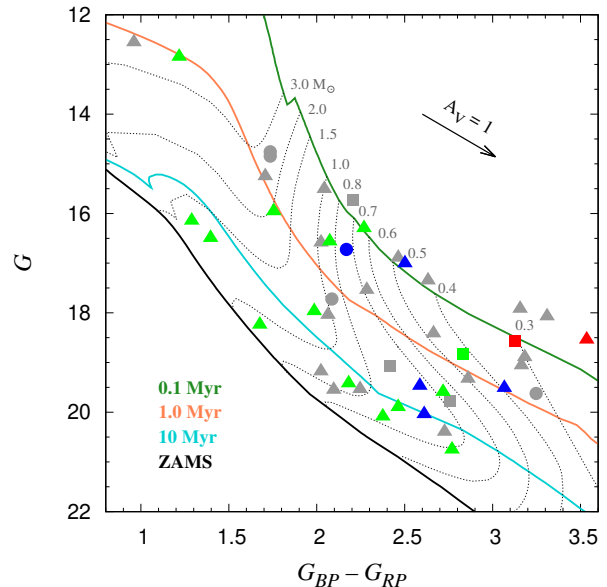


Figure 4. Gaia DR2 color-magnitude diagram of the YSOs (Class I: squares; Class II: triangles; transition-disk: circles) in the subregions Clump A (red), S112 (green), Clump B (blue), and in rest of the region (grey). Overplotted as solid lines are the theoretical isochrones for ages of 0.1, 1.0, and 10 Myr along with the zero-age-main-sequence (ZAMS) taken from the PAdova and TRieste Stellar Evolution Code (Bressan et al. 2012). The evolutionary tracks for different masses (as dotted lines) are also shown. All the isochrones are adjusted for a cluster distance of 2.1 kpc (Blitz et al. 1982) and a universal reddening $A_V \sim 2.78$ mag (Section 3.1).

found. In accordance with the spatial map, the relative number of Class I sources decreases noticeably from the Galactic east to west. Since the Class I sources nor-

mally represent an earlier phase compared to the Class II sources, the ratio of Class I/Class II sources could be used to interpret the evolutionary stage of the subregions, with a higher ratio indicative of a younger population. The source ratio for the subregions Clump A, S112, and Clump B is estimated to be 0.40, 0.36, and 0.25, respectively, varying systematically from east to west. Literature studies of several young and nearby star-forming regions have shown this ratio to vary in a wide range, between ~ 0.1 – 0.8 , with a median of 0.27 (Gutermuth et al. 2009). This suggests that the sources associated with Clump A and S112 subregions consist of younger population and are evolving almost in a similar timescale, while the sources to the western periphery are comparatively older in nature. There is a slight possibility of undercounting of embedded stellar sources toward the western side as the reddening marginally varies compared to the other subregions. In S112, the majority of the YSOs are found to be distributed toward the northern vicinity of BD+45 3216, while the Class I sources have preferentially formed two separate groups both away from the central core. Actually, the S112 subregion itself is fragmented into two dense cores which will be seen in the molecular maps presented later but not resolved here in the Planck data, and these Class I sources nicely coincide with both the cores. As Class I sources have less evolved circumstellar environments, this indicates that star formation is still continuing at those cores. Most probably, these Class I sources are the next-generation stars of the region whose formation is induced by the expansion of the H II region powered by the massive star.

4. MASSIVE STARS AND IONIZED GAS

To investigate the roles massive, ionizing sources play on their surrounding environs, whether to prompt or to restrain subsequent star formation, we present below spectroscopic observations supplemented with infrared imaging data. Furthermore, radio continuum measurements are included to curb the dynamical evolution of the ionized gas associated with the subregions.

4.1. Spectra Classification

Optical spectroscopy for a few bright ($J < 13$ mag) stars toward S112 were conducted to gain knowledge of their stellar properties so as to identify the candidate massive stars as the ionizing sources to influence the surrounding star formation processes via any feedback mechanism. The flux-calibrated normalized spectra of these stars are presented in Figure 6.

Spectral classification is done by comparison with standard spectral libraries (Jacoby et al. 1984; Walborn

& Fitzpatrick 1990; Torres-Dodgen & Weaver 1993), relying on the identification of conspicuous lines and their equivalent widths, following the procedure outlined in Panja et al. (2020). Selected spectral indices are compared with the spectral atlas of Danks & Denefeld (1994), Kobulnicky et al. (2012), and Hernández et al. (2004). Primarily, for early-type stars up to A, we judged by the line strengths of the Balmer series ($H\delta$ 4102 Å, $H\gamma$ 4340 Å, $H\beta$ 4861 Å, $H\alpha$ 6563 Å), He I (5876, 6678, 7065 Å), and He II (4200, 4541, 4686, 5411, 5720 Å). For cooler stars of F or later, we relied on various metallic lines, such as Na I (5890, 5896 Å), Mg I triplet (5167, 5172, 5183 Å), Mg II (4481, 6347 Å), Ca I (6122, 6162 Å), Ca II triplet (8498, 8542, 8662 Å), and Fe I (6495, 7749, 7834 Å). A brief description of the spectral features for each observed star is given as follows.

S1: The star S1 shows prominent He I (4144, 4387, 4471, 5876, 6678, 7065 Å), He II (4541, 4686, 5411 Å), and hydrogen (4101, 4340, 4861, 6563 Å) lines, with an evidence of strong absorption features at He I (5876, 6678, 7065 Å), He II (4541, 5411 Å), and $H\alpha$ (6563 Å) lines, which restricts the spectral type to O as a dwarf. In case of supergiants, the $H\alpha$ line is extremely weak from O5 to B8. The presence of Si II (4128 Å), O III (4415 Å), and a moderate nitrogen enhancement are indicative of later O-type spectra. The line ratio of He I (4471 Å)/He II (4541 Å) is found to be marginally greater than 1, suggesting a spectral type later than O7. Finally, by comparing the equivalent widths of He I (5876 Å), He II (5411 Å), and $H\alpha$ (6563 Å) and a visual comparison of the spectrum with the spectral libraries, we assigned the spectral type of the star as O8 V.

S2: The star S2 shows a peculiar feature of very strong $H\alpha$ (6563 Å) emission, along with strong absorption at Na I (5890, 5896 Å) and Ca II triplet (8498, 8542, 8662 Å). The presence of Ca I (6162 Å), Fe I + Ti I + Cr I (6362 Å), Fe I (6495 Å), and C II (6580 Å) suggests a spectral range between early- to mid-G type. Moreover, the absorption at Mg I triplet (5167, 5172, 5183 Å) is an indication of a G-type spectrum. Comparing the line ratios of $H\alpha$, Na I doublet, and Ca II triplet, we chose the spectral type to be G3 V/III, whereas for the same spectral type the Ca II triplet line strength would be much stronger for a supergiant.

S3: The declining strengths of Na I (5890, 5896 Å), $H\alpha$ (6563 Å), and Ca II triplet (8498, 8542, 8662 Å) in the spectrum suggest a late-F star. From the additional features of Ca II (K) (3933 Å), CH (G band) (4300 Å), and Fe I (4271, 5329, 7749 Å), we determined a spectral type of F7 V/III.

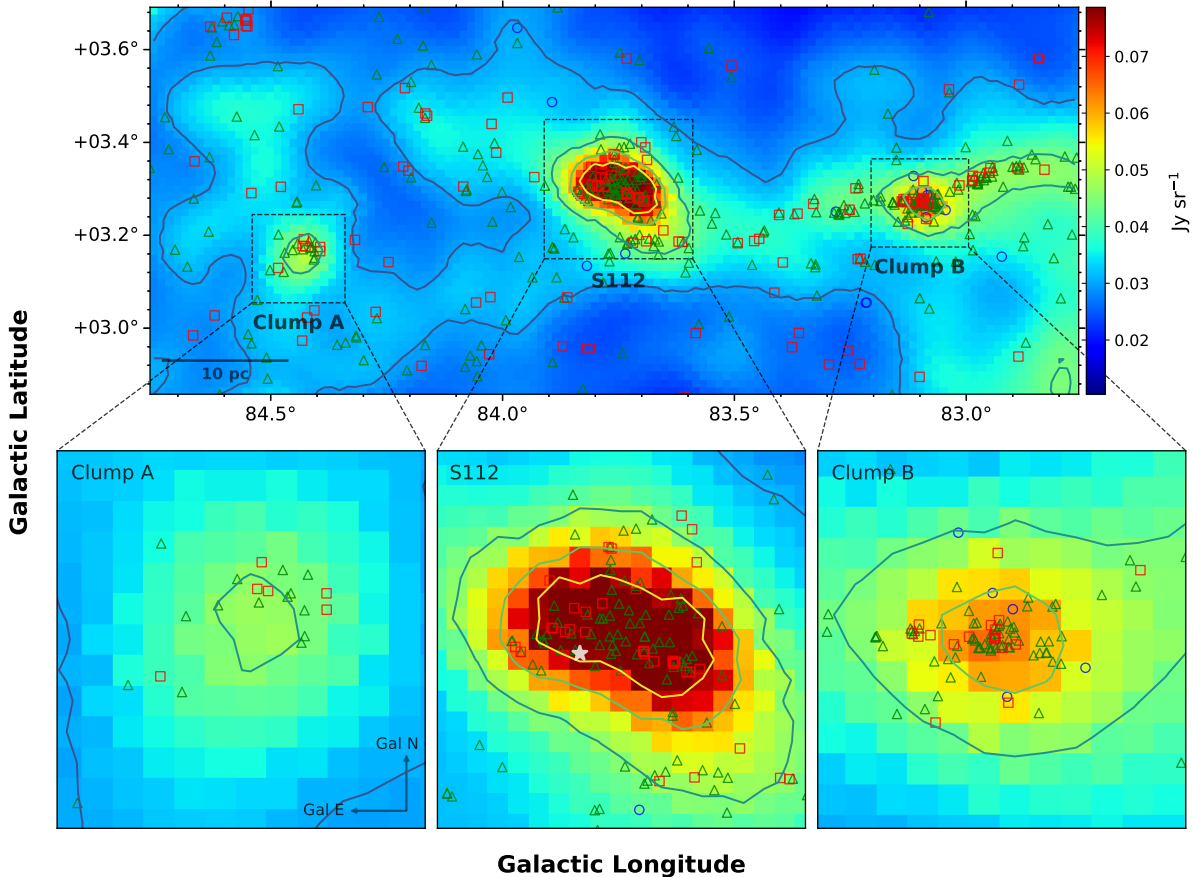


Figure 5. (Top) Spatial distribution of the YSOs (Class I: red square; Class II: green triangle; transition disk: blue circle) overlaid on the Planck 353 GHz map. The stellar density peaks at three subregions (Clump A, S112, and Clump B), and coincide well with the high intensity regions. The contour levels are at 0.028, 0.040, 0.052, and 0.064 Jy sr^{-1} . (Bottom) Zoomed-in maps of the three subregions. The main ionizing source BD+45 3216 is represented by a white asterisk symbol.

S4: The spectrum of S4 exhibits weak presence of He I (5876 Å) and very strong $\text{H}\alpha$ (6563 Å) absorption, indicating a relatively hot star (late-B type). The line ratio of $\text{H}\alpha$ (6563 Å)/He I (5876 Å) suggests a spectral type of B8 or later. Considering the presence of C III + O II (4070 Å), Si III (4552 Å), CN + Fe I (4175 Å), Fe I (4383 Å), and Na I (5890, 5896 Å) features, we assigned the spectral type of this star as B9 V.

S5: This star shows CN + Fe I (4175 Å), Fe I (4532, 6495, 7749 Å), Ca I (6162 Å), and Fe II (6242 Å) blend, which are a signature of late-F types. From the additional features of Na I (5890, 5896 Å), $\text{H}\alpha$ (6563 Å), and Ca II triplet (8498, 8542, 8662 Å), we estimated the spectral type to be F9 V/III.

S6: The spectrum of S6 is similar to that of S4, with presence of weaker He I (5876 Å) and strong $\text{H}\alpha$ (6563 Å) absorption, including C III + O II (4070 Å), CN + Fe I (4175 Å), Si II (4128 Å), Si IV (4089 Å), Mn I + Fe I (4458 Å), and N III (4511 Å). Considering the line

strength of $\text{H}\alpha$ (6563 Å)/He I (5876 Å), we classified the star as a B9.5–A0 V type.

All the classified stars are primarily placed into the dwarfs/giants categories. With our low-dispersion spectroscopy, the typical uncertainty for early-type stars up to the A type is ± 1 subtype, whereas for F-type and later the uncertainty is about ± 3 subtypes. However, the distribution of varying reddening and the contribution from circumstellar dust emission can have considerable effects on the nature of spectral class, as will be discussed in the next section.

4.2. Reddening and Membership of the Observed Stars

Stellar parameters were derived from the estimated spectral types and the infrared photometry. To estimate the A_V of each source, we utilized the JHK color excess relations (Panja et al. 2020), adopting the reddening laws in Cohen et al. (1981) and the intrinsic stellar colors from Martins & Plez (2006) for the O-type star and from Pecaut & Mamajek (2013) for other sources.

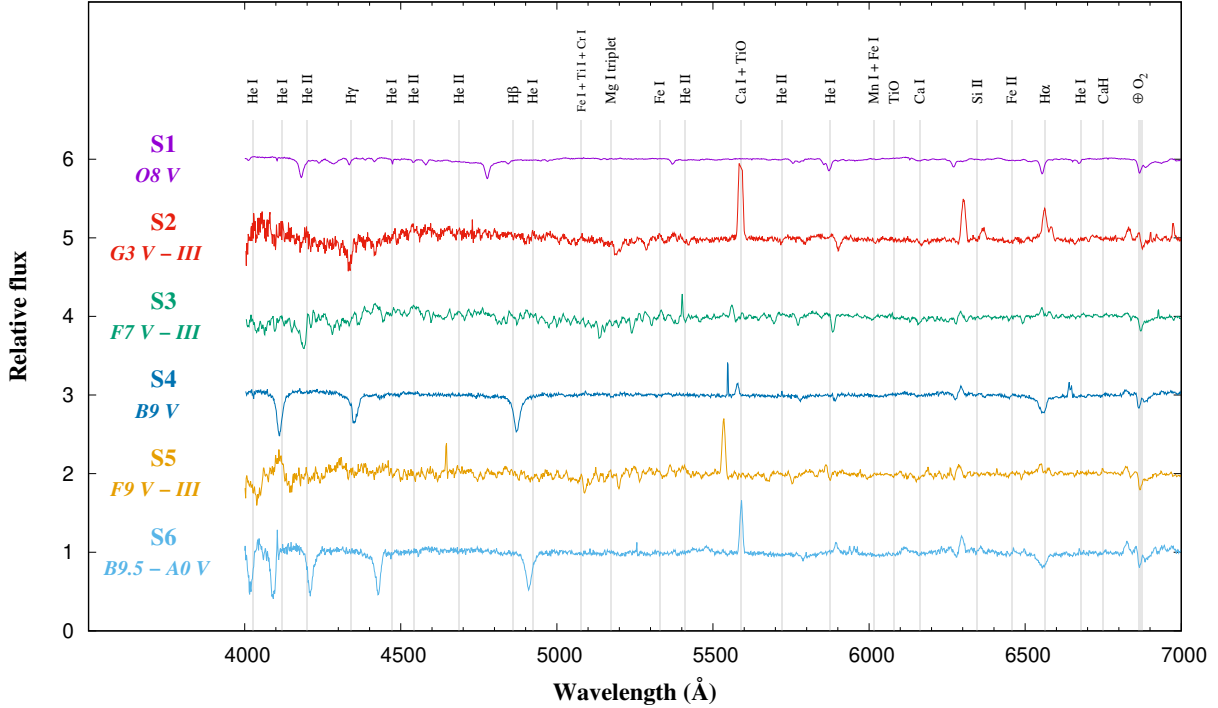


Figure 6. Flux-calibrated normalized spectra of the stars toward S112. Prominent spectral line are marked.

Furthermore, the position of a particular source in a color-color diagram provides a consistency check of its reddening.

Table 3 lists the stellar parameters of the spectroscopically observed targets. The positions in the 2MASS color-color diagram, shown in Figure 7 (left), can be accounted for either with extinction, i.e., A_V of 3.2–3.8 mag for S3 and S5, and 2.5 mag for S2, or as excess emission for S1, S4, and S6 arising from thermal bremsstrahlung of these early-type stars.

The spectroscopic distance of each source, namely being derived from the spectroscopically determined extinction, apparent (JHK) and absolute magnitudes (Pecaut & Mamajek 2013) are by and large confirmed by those computed from the Gaia DR2 parallax using the estimates by Bailer-Jones et al. (2018). As seen in Table 3, the distances are all consistent with being cluster members. Noteworthily the Gaia DR2 distance of BD+45 3216 (S1) is $1.822^{+1.704}_{-0.705}$ kpc, whereas Gaia EDR3 has resolved both components of the source with relatively precise parallaxes (0.4229 ± 0.0477 mas and 0.4094 ± 0.0394 mas), which correspond to geometric distances of $2.248^{+0.275}_{-0.226}$ kpc and $2.456^{+0.271}_{-0.274}$ kpc (Bailer-Jones et al. 2021).

Our spectroscopic observations yielded only a single massive (O8 V) star capable of producing sufficient ultraviolet radiation, and responsible for creating and sustaining the ionized region. A color composite image of

the S112 region is presented as Figure 7 (right), generated with a combination of near- to mid-infrared wavebands, highlighting the locations of the spectroscopically observed stars. A vivid rim-like structure, shaped semi-circularly, surrounding which trails of dust are prominent. To the north, multiple filaments are seen interlaced with diffuse nebulosity, within which a significant amount of dust is contained. The stellar feedback by the main illuminating source BD+45 3216, i.e., S1 and the physical mechanism in formation of the bright arc-like structure are discussed in detail by Panwar et al. (2020). They have proposed a triggered star formation scenario as an outcome of the encounter between the ionized gas and molecular cloud for this blister-shaped H II region.

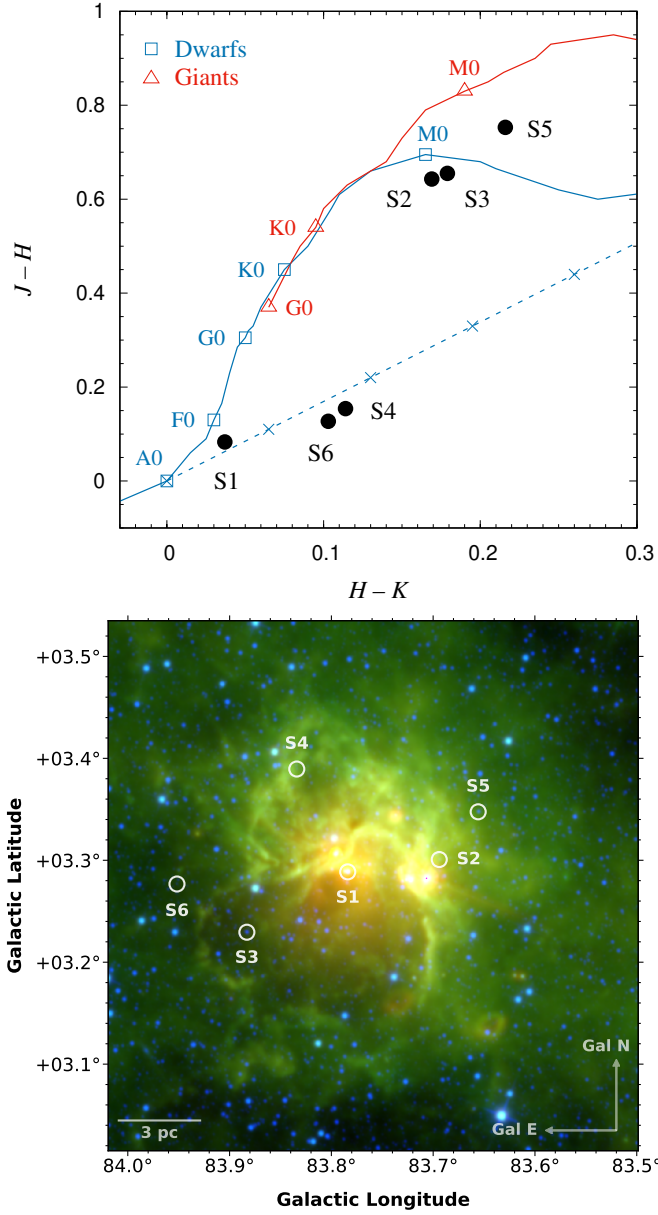


Figure 7. (left) The 2MASS color-color diagram for the spectroscopically observed stars, each marked with a black filled circle, overlaid with the unreddened main-sequence (blue solid line) and giant loci (red solid line), both taken from *Bessell & Brett (1988)*. A reddening vector drawn from the tip of the main sequence, i.e., from A0 is represented by the blue dashed line, along which the consecutive cross symbols indicate an increment of reddening of $A_V = 1$ mag. (right) Color composite image of S112 created with WISE W_4 ($22 \mu\text{m}$ in red), W_3 ($12 \mu\text{m}$ in green), and W_1 ($3.4 \mu\text{m}$ in blue) bands. Spectroscopically observed sources are marked (white circles) and labelled.

Table 3. Parameters of the Spectroscopically Observed Stars

Star	2MASS Designation	Glcn. (deg)	Glat. (deg)	J (mag)	H (mag)	K (mag)	Exposure Time (s)	Spectral Type	Spectroscopic A_V (mag)	Distance (kpc)	Gaia DR2 Distance (kpc)
S1	2MASSJ20335033 + 4539412	083.783904	+03.288649	8.182 ± 0.019	8.099 ± 0.020	8.062 ± 0.020	300	O8 V	1.916 ± 0.065	1.965 ± 0.154	1.822 $+1.704$ -0.705
S2	2MASSJ20332868 + 4535473	083.694004	+03.300749	12.870 ± 0.021	12.227 ± 0.021	12.058 ± 0.019	1500	G3 V/III	2.509 ± 0.128	...	1.971 $+0.092$ -0.084
S3	2MASSJ20342691 + 4542206	083.883029	+03.229439	10.836 ± 0.020	10.181 ± 0.021	10.002 ± 0.018	1200	F7 V/III	3.206 ± 0.191	...	1.990 $+0.064$ -0.060
S4	2MASSJ20333266 + 4545419	083.834016	+03.389542	12.920 ± 0.024	12.766 ± 0.029	12.652 ± 0.030	1200	B9 V	1.693 ± 0.081	2.158 ± 0.238	2.044 $+0.076$ -0.071
S5	2MASSJ20330798 + 4535366	083.655728	+03.347573	11.079 ± 0.020	10.326 ± 0.019	10.110 ± 0.016	1200	F9 V/III	3.823 ± 0.204	...	2.049 $+0.073$ -0.068
S6	2MASSJ20342791 + 4547203	083.951724	+03.276741	12.942 ± 0.020	12.815 ± 0.024	12.712 ± 0.024	1200	B9.5-A0 V	1.426 ± 0.056	2.214 ± 0.199	1.985 $+0.072$ -0.067

4.3. Properties of the Ionized Gas

Compact H II regions are distinct free-free radio sources. The NVSS 1.4 GHz radio continuum observations hence allow us to estimate the physical parameters of the ionized gas associated with the subregions. The radio continuum distribution, overlaid on a far-infrared 160 μm map for the three subregions, is shown in Figure 8 and the parameters thus derived are given in Table 4. The number of Lyman continuum photons (N_{UV}), considering an optically thin, homogeneous and spherical H II region, is given by (Matsakis et al. 1976)

$$N_{UV}[\text{s}^{-1}] = 7.5 \times 10^{46} \left(\frac{S_\nu}{\text{Jy}}\right) \left(\frac{D}{\text{kpc}}\right)^2 \times \left(\frac{T_e}{10^4 \text{ K}}\right)^{-0.45} \left(\frac{\nu}{\text{GHz}}\right)^{0.1} \quad (1)$$

where S_ν is the integrated 1.4 GHz flux density in Jy, D is the distance in kpc, T_e is the electron temperature, and ν is the frequency in GHz. Adopted values are the measured radio fluxes listed in Table 4, a distance of 2.1 kpc (Table 3), and an electron temperature of 10^4 K (Matsakis et al. 1976).

For Clump A ($\ell = 084^\circ 4325$; $b = +03^\circ 1598$), little 1.4 GHz radio emission is detected therefore no parameters of ionized gas are available in Table 4. Esimbek et al. (2008) also have reported that this relatively cold core does not show any evidence of H II emission, with no presence of MSX (Egan et al. 2003) or IRAS (Neugebauer et al. 1984) point sources. In lieu, Clump A is designated as a cold core in the Planck Catalogue of Galactic Cold Clumps (PGCC G084.43+03.16; Planck Collaboration et al. 2016), which are good candidates for studies of the early evolutionary stages of star formation. In S112, on the other hand two radio peaks are distinct, though the main exciting star (BD+45 3216) coincides with neither of the peaks. Within this region two MSX sources (MSX G083.7071+03.2817 and MSX G083.7962+03.3058) are located and their interaction with the region is discussed in detail by Panwar et al. (2020). Studying both the ionized gas and the molecular cloud in association with the MSX sources near the massive star BD+45 3216, they have proposed a sequential star formation scenario. Clump B shows a single and definite maximum with a moderate ionization level. Urquhart et al. (2009) have presented the Red MSX Source (RMS) survey, programmed to detect the massive young stellar candidates in the northern hemisphere using the Very Large Array (VLA) high resolution radio continuum observations at 6 cm. They have detected radio emission with an integrated flux of 101 mJy from the H II region associated with Clump B

and catalogued the region as VLA G083.0934+03.2720 with a MSX counterpart as MSX G083.0936+03.2724. Also Anderson et al. (2015) has mentioned this H II region as G083.097+03.270 with an ionized gas velocity of -7.1 km s^{-1} traced by the radio recombination lines.

Using the Lyman continuum flux to estimate the spectral class of a single ionizing star (Panagia 1973), in S112 it would be O9.5–B0 V, which is in close agreement with our spectroscopic determinations (O8 V). Evidently from Figure 8 the coincidence of dust emission with radio continuum differs: in S112, both emissions near BD+45 3216 are comparatively devoid, indicating the H II region to be exclusively powered by BD+45 3216. In contrary, in Clump B a higher intensity plus the compact morphology points to the possibility of ionization caused by a group of early-B type stars still embedded in the cloud, rather than a single O-type star alone (Martín-Hernández et al. 2003). Based on the infrared luminosity function, Ivanov et al. (2005) too suggested that Clump B hosts a concentration of about half a dozen ionizing stars. This conforms to the notion that OB stars often exist in binaries or groups.

The size of the ionized gas as a function of the the total Lyman photons and the gas density is known as the Strömgen radius (R_s), given by

$$R_s = (3N_{UV}/4\pi n_0^2 \alpha_B)^{1/3}, \quad (2)$$

where the radiative recombination coefficient $\alpha_B = 2.6 \times 10^{-13} (10^4 \text{ K}/T_e)^{0.7} \text{ cm}^3 \text{ s}^{-1}$ (Kwan 1997), and n_0 is the initial particle number density of the ambient neutral gas, typically $n_0 \sim 10^3 \text{ cm}^{-3}$.

The dynamical age (t_{dyn}) of an H II region is computed using the relation (Dyson & Williams 1980):

$$t_{dyn} = \left(\frac{4R_s}{7c_s}\right) \left[\left(\frac{R_{\text{HII}}}{R_s}\right)^{7/4} - 1 \right], \quad (3)$$

where $c_s = 11 \text{ km s}^{-1}$ is the isothermal sound speed in the ionized gas (Bisbas et al. 2009), and R_{HII} is the radius of the H II region. Adopting values in Table 4, the dynamical age of the H II regions is found to be 0.18–1.0 Myr, which is consistent with our earlier estimates (Section 3.4). The S112 region appears relatively evolved compared to the other two, though varying dust density may induce substantial changes in the dynamical age determination.

5. MOLECULAR CLOUD MORPHOLOGY

We now present the molecular cloud parameters derived from the CO data. The molecular gas traced by

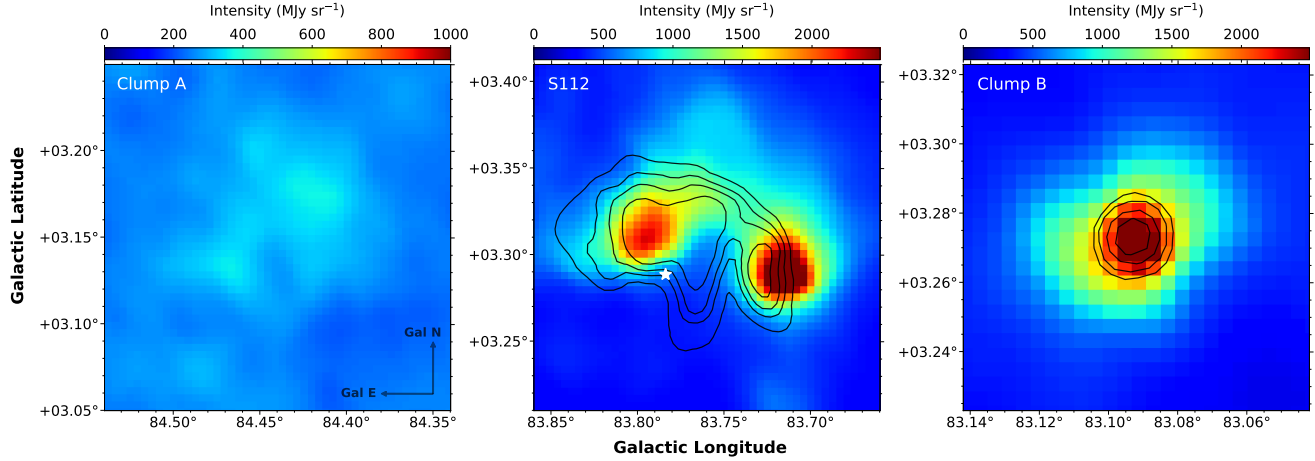


Figure 8. The AKARI 160 μm emission (false color), superimposed with the NVSS 1.4 GHz radio continuum (contours) for Clump A, S112, and Clump B. For Clump A, no 1.4 GHz emission is detected. The contour levels for S112 are at 0.003, 0.010, 0.020, and 0.040 Jy/beam, whereas the contour levels for Clump B are at 0.003, 0.006, 0.012, and 0.020 Jy/beam. The main illuminating source BD+45 3216 is indicated by a white asterisk symbol.

Table 4. Physical parameters of the ionized gas associated with the subregions

Region	Glon.	Glat.	R_{HII}	S_ν	N_{UV}	$\log(N_{UV})$	Star	R_s	t_{dyn}
	(deg)	(deg)	(pc)	(mJy)	(s^{-1})		type	(pc)	(Myr)
S112	083.7589	+03.2750	3.038	1414	4.836×10^{47}	47.684	O9.5–B0 V	0.2473	1.023
Clump B	083.0890	+03.2693	0.668	32.39	1.108×10^{46}	46.044	B0.5–B1 V	0.0702	0.184

^{12}CO reveals structures of gas (density $\sim 10^2 \text{ cm}^{-3}$), whereas the optically thinner ^{13}CO or C^{18}O line traces denser ($\sim 10^3\text{--}10^4 \text{ cm}^{-3}$) parts of the cloud. A combination of ^{12}CO , ^{13}CO , and C^{18}O isotopologues thus provides complementary information of the molecular cloud morphology, from cloud envelopes to denser segments as giant molecular clouds, to cloud fragments to pre-stellar cores, and of cloud physical/chemical conditions. The detailed methodology to derive the cloud parameters from these observations are given in Sun et al. (2020).

5.1. Intensity Distribution

A color composite map of the integrated intensity in the velocity interval of -33 to 15 km s^{-1} , constructed with a combination of three CO isotopologues is presented in Figure 9. Large-scale extended structures are prominent in ^{12}CO emission, whereas in the ^{13}CO map, intricate filaments are seen connecting the subregions Clump A and S112, along which Class I objects are detected (see the YSO distribution in Figure 5). The complete filament extends over $\sim 80 \text{ pc}$ parallel to the Galactic plane, along which cloud fragments/cores in addition to the three subregions are located. The C^{18}O

emission is detected mostly at the location of the three subregions, where the compact structures are. A summary of the molecular cloud parameters for the three subregions is presented in Table 5.

5.2. Velocity Distribution

The overall velocity distribution (longitude-velocity map) of molecular gas within the mapped region is displayed as Figure 10. The velocity range ($[-33, 15] \text{ km s}^{-1}$) for the complete molecular structure is relatively wide. Therefore, the cloud structures are studied in three velocity channels in $[-33, -10] \text{ km s}^{-1}$, $[-10, +6.5] \text{ km s}^{-1}$, and $[6.5, 15] \text{ km s}^{-1}$, where prominent emission is detected. The velocity structures for the three channels are shown in Figure 11. For C^{18}O , significant emission is detected only in the $[-10, 6.5] \text{ km s}^{-1}$ channel. Clearly the velocity channels of $[-33, -10] \text{ km s}^{-1}$ and $[6.5, 15] \text{ km s}^{-1}$ are not consistent with the cloud distribution, and hence the preferred velocity range of the molecular cloud would be $[-10, 6.5] \text{ km s}^{-1}$.

The velocity and its dispersion maps are displayed in Figure 12 for ^{12}CO , Figure 13 for ^{13}CO , and Figure 14 for C^{18}O . The moment 1 (velocity) map in ^{12}CO

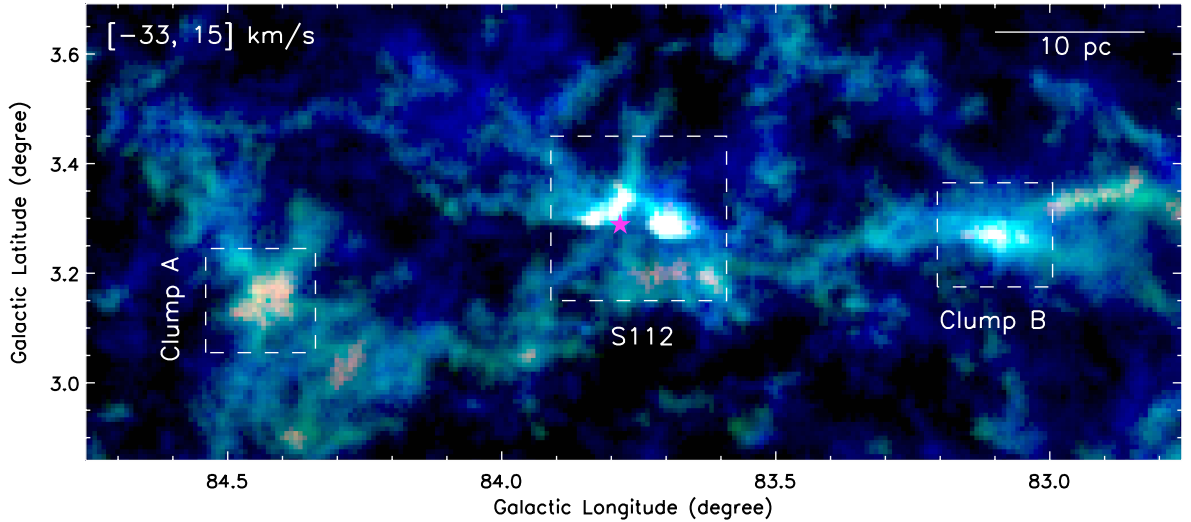


Figure 9. Integrated intensity map (moment 0) over the velocity range $[-33, 15]$ km s^{-1} , created with a combination of ^{12}CO (blue), ^{13}CO (green), and C^{18}O (red). Each of the three subregions is marked with a dashed rectangle. The principal ionizing star BD+45 3216, located within the S112 subregion, is indicated by an asterisk symbol.

shows considerable velocity gradient from Galactic east to west. Toward the Galactic east, velocity varies almost uniformly between -2.5 and -5.0 km s^{-1} with an average of -3.6 km s^{-1} , whereas in the Galactic west, the velocity fluctuates more, except along the filamentary axis where the velocity remains ~ -2.5 km s^{-1} . The velocity dispersion (moment 2) is also lower (average ~ 3.2 km s^{-1}) in the Galactic east and increases slightly (average ~ 3.8 km s^{-1}) to the west.

The moment 1 map of ^{13}CO , being optically thinner, traces readily the molecular cloud distribution. The velocity varies almost consistently along the entire filamentary structure from -4.0 km s^{-1} (east) to -2.5 km s^{-1} (west). The velocity dispersion is also much smaller, averaging ~ 1.8 km s^{-1} , compared to that of ^{12}CO . Similar results apply to the C^{18}O map, where the velocity increases gradually from the Galactic east to west.

In the velocity dispersion maps of ^{13}CO (Figure 13(b)) and C^{18}O (Figure 14(b)), the overlap of three MSX sources mentioned in Section 4.3 are shown. Interestingly the regions of elevated velocity dispersion nicely coincide with all the MSX source positions. Toward S112, Maud et al. (2015) reported massive ($27.6 M_{\odot}$) molecular outflow associated with MSX G083.7071+03.2817 having $V_{lsr} = -3.2$ km s^{-1} . Another source MSX G083.7962+03.3058 is less massive ($5.0 M_{\odot}$) and shows some evidence of outflow with $V_{lsr} = -3.7$ km s^{-1} . Panwar et al. (2020) also mentioned probable association of molecular gas with these outflow sources. In the study of Maud et al. (2015), toward Clump B, MSX G083.0936+03.2724 is highly lu-

minous ($12 \times 10^3 L_{\odot}$) and is relatively massive ($7.7 M_{\odot}$) showing clear signature of molecular outflow with $V_{lsr} = -3.0$ km s^{-1} . These spatial and kinematic correlation between the outflows and the molecular gas imply that the high velocity dispersions are most probably related and caused by these outflows. The outflow sources have dynamical timescales of $3\text{--}4 \times 10^4$ yr.

5.3. Column Density Distribution

The distribution of the excitation temperature, derived from ^{12}CO assuming an optically thick condition, is presented in Figure 15(a). Along the filamentary cloud, the excitation temperature varies steadily with an average value of ~ 10 K, which is similar to the typical kinetic temperature of molecular clouds, peaking near the three subregions, with the warmest for Clump B (32.5 K), followed by S112 (28.6 K) and Clump A (13.7 K). The optical depths are presented in Figure 15(b) for ^{13}CO and in Figure 15(c) for C^{18}O . The optical depths are then used to make saturation corrections to the column densities.

The H_2 column density is derived by adopting a CO-to-H_2 conversion factor, namely $X_{\text{CO}} \equiv 2 \times 10^{20} \text{cm}^{-2} (\text{K km s}^{-1})^{-1}$ for ^{12}CO and by assuming local thermodynamic equilibrium and abundance ratios of H_2 to CO for ^{13}CO and for C^{18}O . The H_2 column density map for the CO triplet is shown in Figure 16. Within S112 and Clump B, the column density varies on the order of 4–6 times 10^{21}cm^{-2} , with the highest values ranging between 3–6 times 10^{22}cm^{-2} .

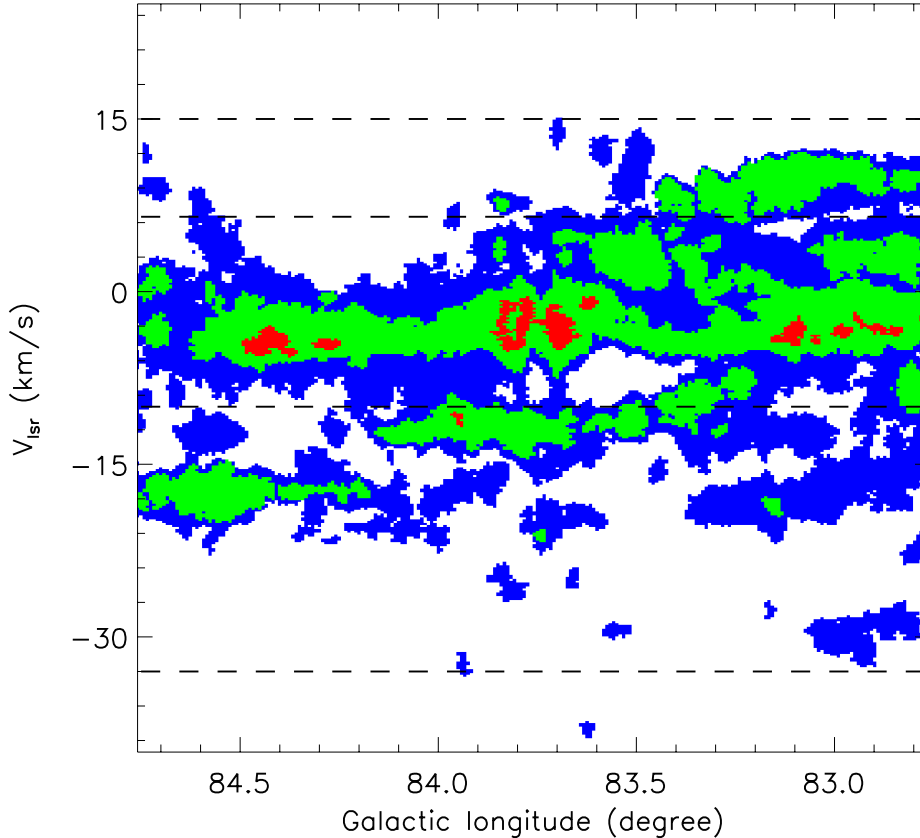


Figure 10. Longitude-velocity ($\ell - V$) map of the entire field toward S112, integrated over the Galactic latitude range of $b = [2^{\circ}8583, 3^{\circ}6917]$. The blue, green, and red colors indicate ^{12}CO , ^{13}CO , and C^{18}O emission, respectively. The four horizontal dashed lines denote $V_{lsr} = -33, -10, 6.5,$ and 15 km s^{-1} .

The corresponding values are relatively lower in Clump A, averaging 2–3 times 10^{21} cm^{-2} , peaking about $\sim 7.5 \times 10^{21} \text{ cm}^{-2}$. For the results presented here, the C^{18}O emission is relatively discrete due to less velocity crowding and line blending (Su et al. 2019), in comparison with the extended ^{12}CO and ^{13}CO emission. Therefore, the C^{18}O emission is useful in detecting the denser components, which are mainly associated with cloud cores.

To combine the facts that we found prominent star formation activity mostly at the higher column density zones. These results seem well consistent with the simulated analysis of Clark & Glover (2014) according to which in the local interstellar medium the star formation is only possible when the area-averaged gas column density exceeds 10^{21} cm^{-2} . Consequently similar results have been observationally obtained by Das et al. (2021) showing the correlation between star formation rate and gas column density in the Milky Way clouds.

5.4. Molecular Mass

Next we have derived the molecular cloud mass for the CO isotopologues from the integrated column density maps by adopting the velocity range $[-33, 15] \text{ km s}^{-1}$ and a distance of 2.1 kpc. The H_2 mass are obtained by assuming a constant CO-to- H_2 conversion factor of $2 \times 10^{20} \text{ cm}^{-2} (\text{K km s}^{-1})^{-1}$ (Bolatto et al. 2013) for ^{12}CO and local thermodynamic equilibrium (LTE) and abundance ratios of H_2 to ^{13}CO for ^{13}CO , respectively (Sun et al. 2020).

We found the ^{13}CO mass of Clump A as $2.58 \times 10^3 M_{\odot}$. Whereas Esimbek et al. (2008) have computed the ^{13}CO cloud mass as $M_{LTE} = 4.37 \times 10^3 M_{\odot}$ with a virial parameter of 0.25, which is well below the threshold value ($\lesssim 2$) for the onset of collapse of supercritical cloud fragments (Kauffmann et al. 2013). Note, however, that the low virial parameters for massive molecular clumps could be an artifact (Singh et al. 2021). In the PGCC catalogue (Planck Collaboration et al. 2016), the mass of PGCC G084.43+03.16 associated with Clump A was

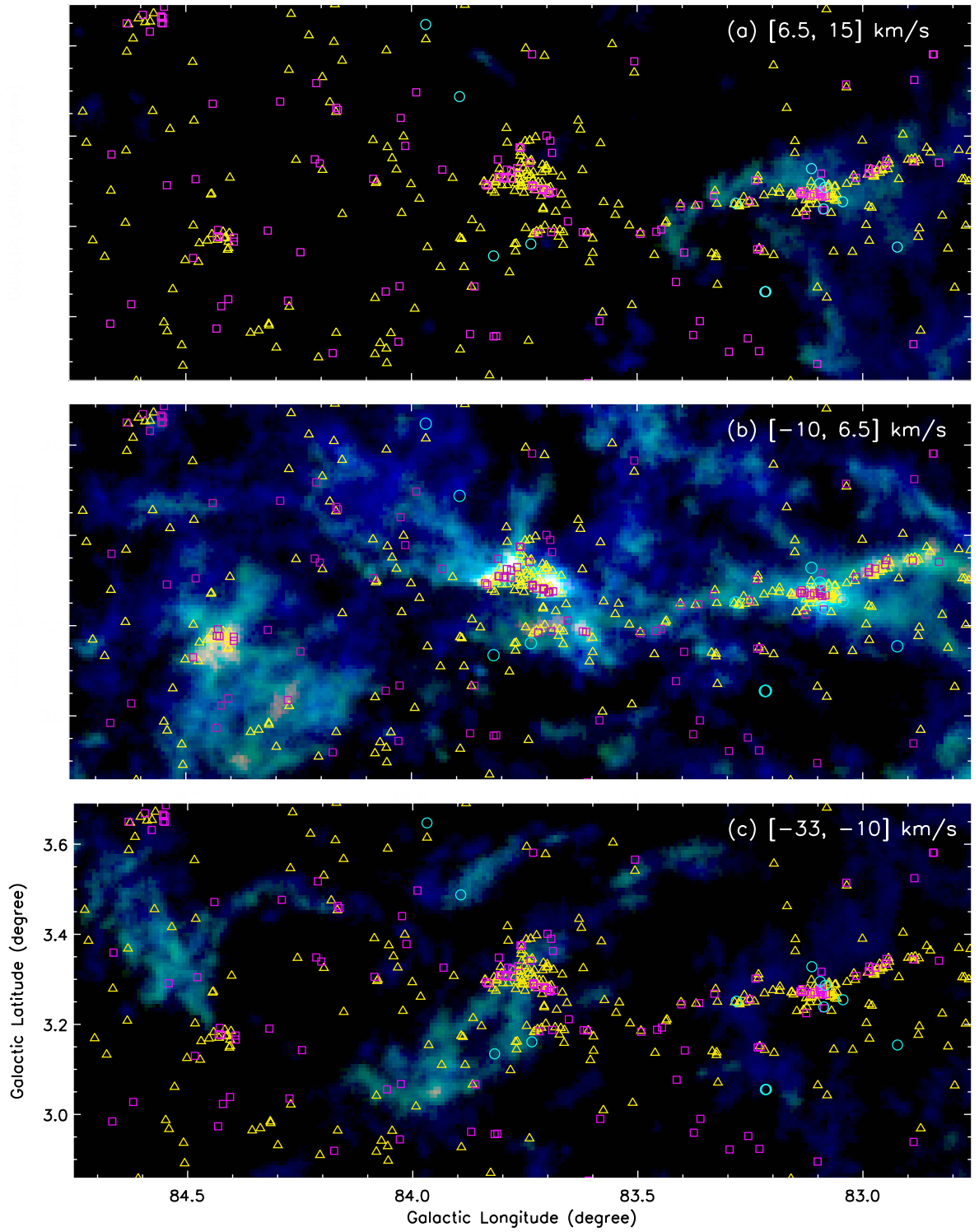


Figure 11. The channel maps for ^{12}CO (blue), ^{13}CO (green), and C^{18}O (red) with the velocity range depicted in each panel. Overplotted are the YSOs (Class I: squares; Class II: triangles; transition disk objects: circles).

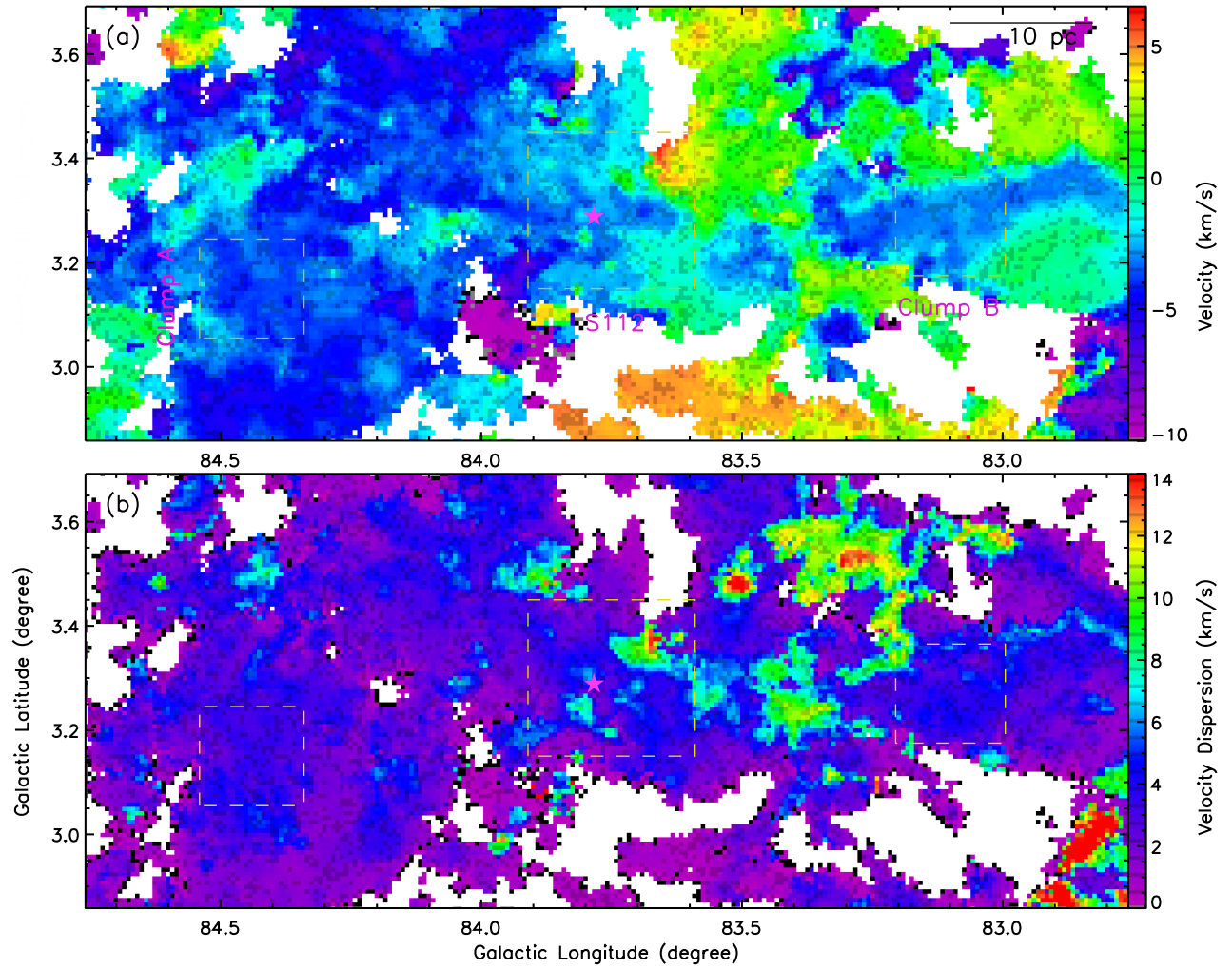


Figure 12. Velocity (moment 1) and velocity dispersion (moment 2) maps for ^{12}CO in the velocity range $[-10, 6.5]$ km s $^{-1}$.

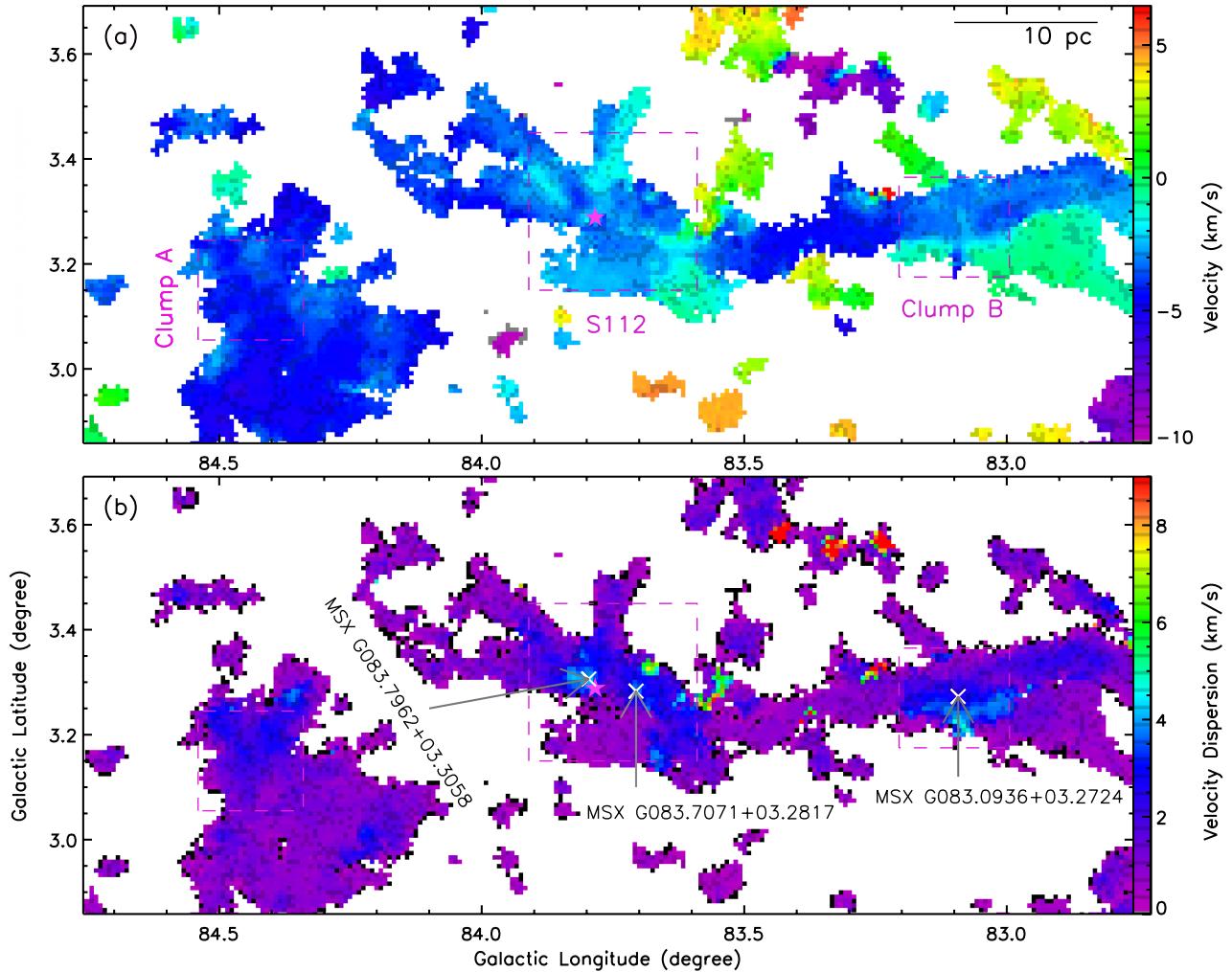


Figure 13. Moment 1 and moment 2 maps for ^{13}CO . The MSX sources, two in S112 and another in Clump B are overlaid with cross symbols.

computed to be $4.30 \times 10^3 M_{\odot}$, based on an overestimated distance of 4.26 kpc. But considering a proper clump distance of 2.1 kpc, the rescaled mass turns to be $\sim 1.03 \times 10^3 M_{\odot}$. Dobashi et al. (1994) mentioned the molecular cloud as 084.4+03.2 and obtained similar kinematic parameters. In spite of significant deviations in the previously estimated masses, these results so far indicate that Clump A is indeed a high-mass star forming region which is in the earliest of its evolutionary phase.

S112 is a massive clump with a total ^{13}CO mass of $9.02 \times 10^3 M_{\odot}$. This clump merges with the molecular cloud 083.7+03.3 listed in Dobashi et al. (1994).

The molecular mass of Clump B estimated from ^{13}CO is $4.27 \times 10^3 M_{\odot}$. By and large, Clump B has the possibility to be associated with the molecular cloud 083.1+03.3 from Dobashi et al. (1994), separating in angular scale of $\sim 2.16'$. Their cloud also depicts kinematic velocity

($V_{lsr} = -3.3 \text{ km s}^{-1}$) and distance (2.1 kpc) similar to those in Clump B.

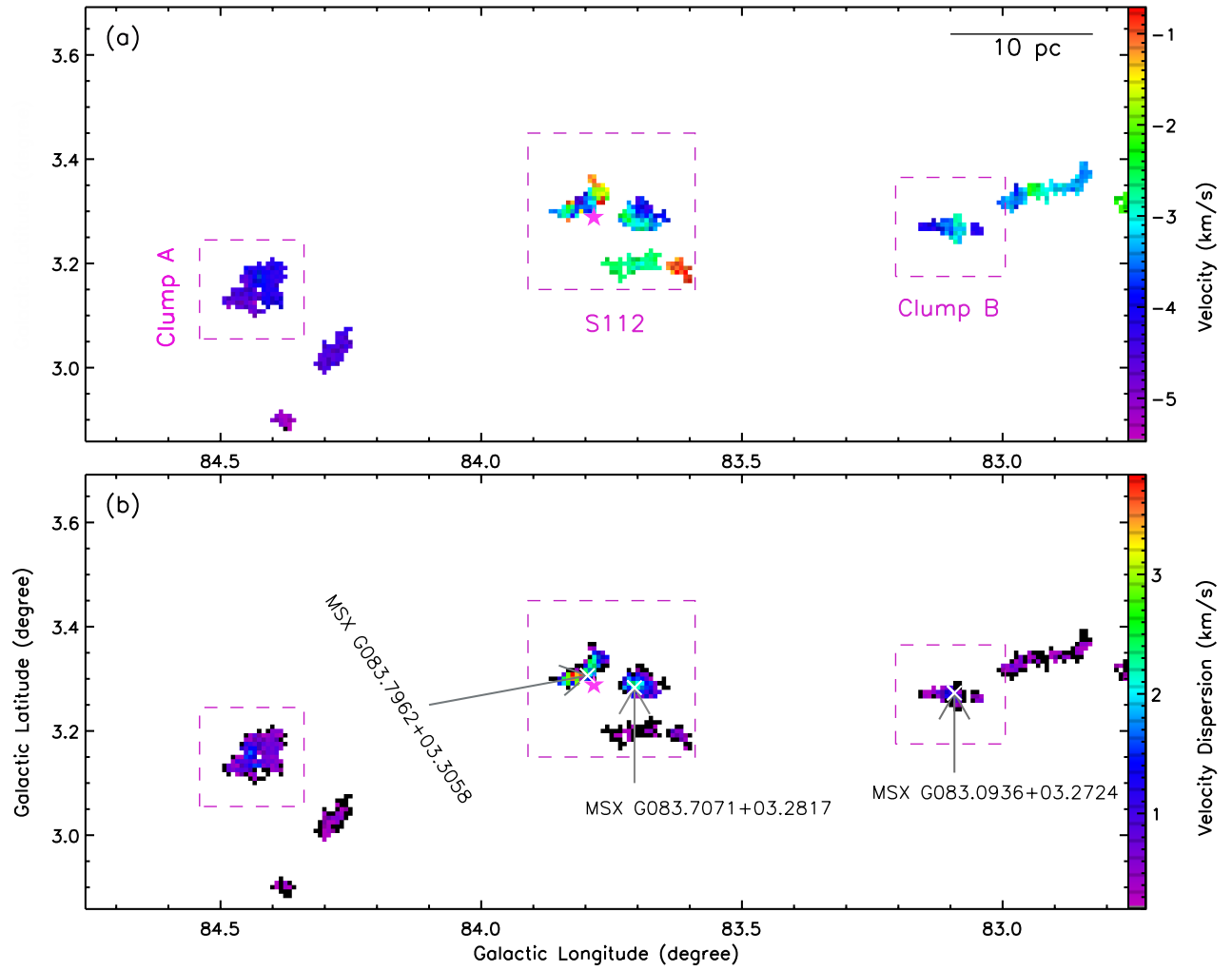


Figure 14. Moment 1 and moment 2 maps for $C^{18}O$.

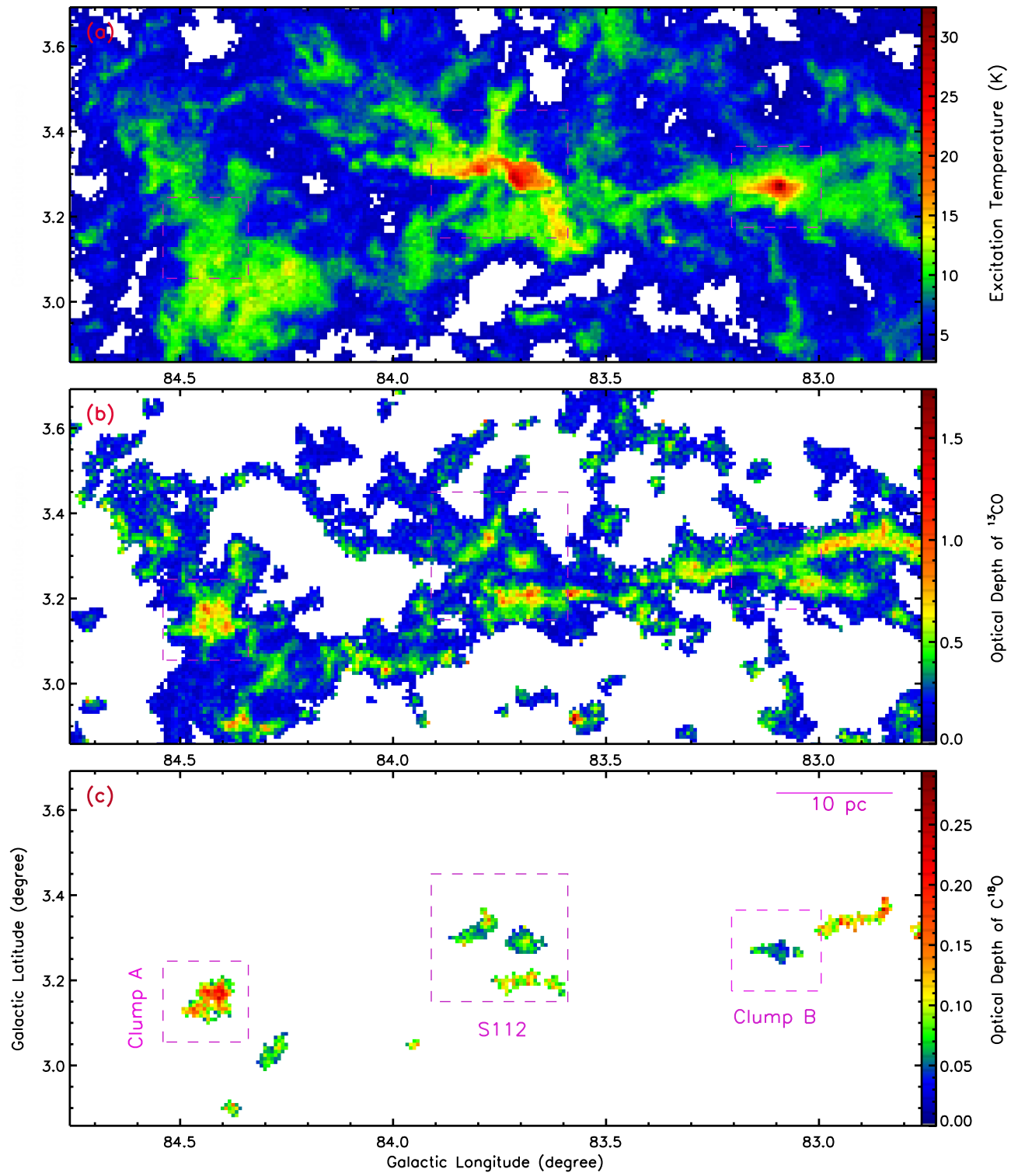


Figure 15. (a) Excitation temperature map for ^{12}CO ; optical depths for (b) ^{13}CO and for (c) C^{18}O .

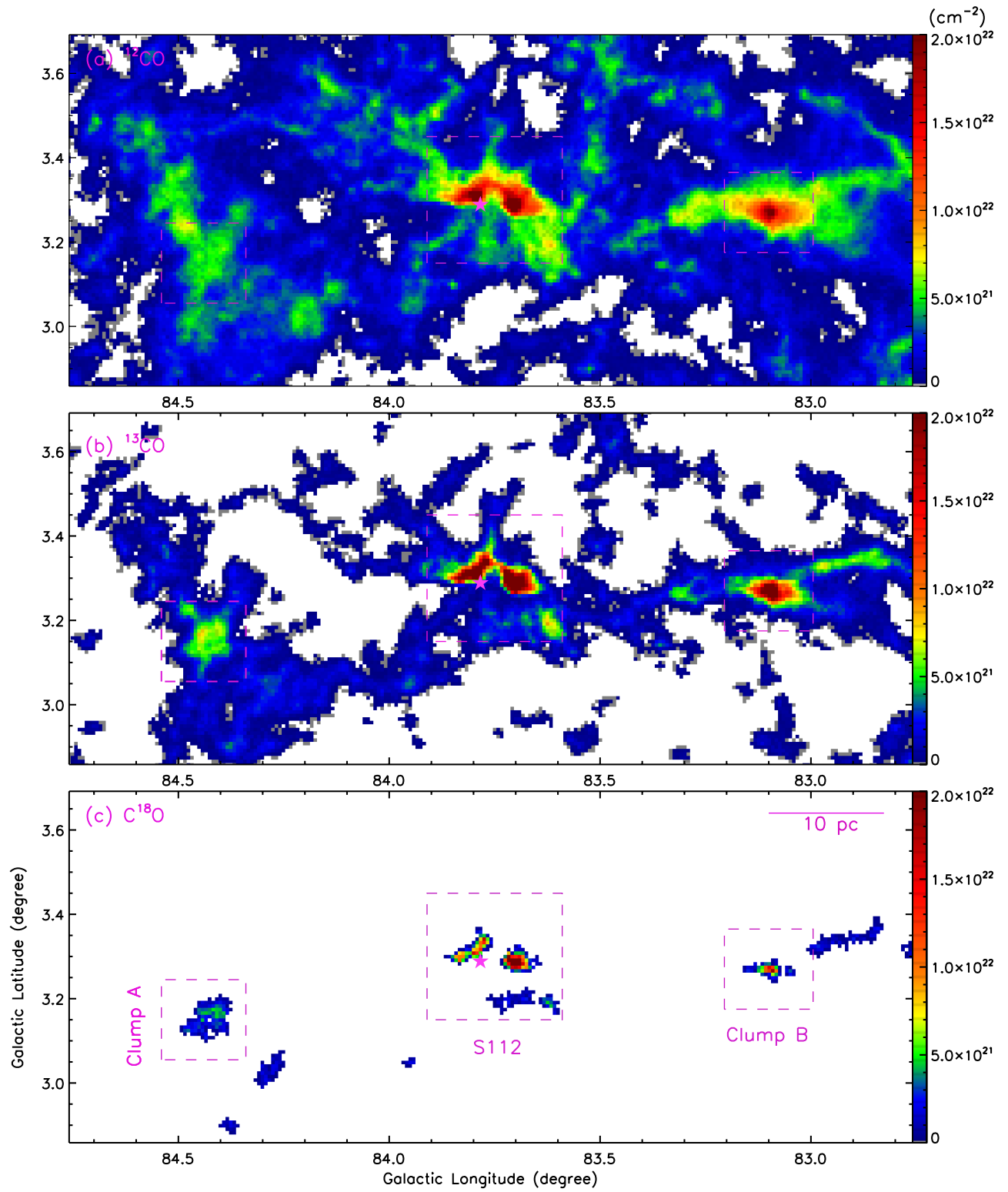


Figure 16. The H_2 column density distribution for ^{12}CO , ^{13}CO , and $C^{18}O$, respectively.

Table 5. Parameters of the molecular clouds associated with the subregions

CO Survey	Intensity (K km s ⁻¹)		Velocity (km s ⁻¹)	Velocity Dispersion (km s ⁻¹)	Excitation Temperature (K)	Optical Depth		H ₂ Column Density (10 ²¹ cm ⁻²)	H ₂ Mass (10 ³ M _⊙)	
	Peak	Mean				Peak	Mean			
Clump A (0°20 × 0°19)										
¹² CO	35.68	18.03	-3.60	3.23	13.68	9.12	...	7.14	3.61	4.13
¹³ CO	9.82	3.08	-4.02	1.64	0.33	7.82	2.25	2.58
S112 (0°32 × 0°30)										
¹² CO	158.73	23.75	-2.36	3.88	28.61	10.06	...	31.75	4.75	13.84
¹³ CO	37.40	3.19	-2.61	1.72	0.25	64.90	3.10	9.02
Clump B (0°21 × 0°19)										
¹² CO	105.11	29.48	-2.48	3.85	32.46	10.29	...	21.02	5.90	6.73
¹³ CO	27.38	4.04	-2.55	1.96	0.32	49.78	3.74	4.27

5.5. Star Formation Activity in the Filamentary Complex

We now discuss the global star formation processes in the region. The YSOs are found exclusively at higher column density zones, which themselves are interconnected via filaments. The extinction pattern resembles the molecular cloud morphology. This supports the notion of the “hub-filament” configuration where a hub, i.e., the conjunction of filaments along which, likely via magnetic fields, material channels to seed the formation of massive stars or star clusters (Kumar et al. 2022). The velocity measurements reveal the cloud geometry and kinematics. Considering a median cloud velocity of ~ -3.65 km s $^{-1}$ in ^{13}CO , the axisymmetric Galactic rotation model (Reid et al. 2019) produces a kinematic distance of $\sim 1.52 \pm 0.12$ kpc (local arm), marginally closer than that ($\sim 1.76 \pm 0.14$ kpc) of the main exciting star. In the velocity channel maps (Figure 11), considerable amount of cloud structures were detected in the channels of $[-33, -10]$ km s $^{-1}$ and $[6.5, 15]$ km s $^{-1}$. The Galactic rotation model suggests these to be either background (distance $\gtrsim 3.0$ kpc) or foreground (distance $\lesssim 1.3$ kpc) clouds located along the same line-of-sight, although given the uncertainties in the distances the possibility of relation between these clouds cannot be ruled out. A plausible explanation for the velocity gradient across the filamentary cloud is that the cloud distance varies, i.e., the eastern side cloud is tilted farther away compared to the western side.

The higher fraction of Class I objects toward the Galactic east indicates that the western side is relatively more evolved. It is therefore proposed that star formation begun in the west, then propagated to the east along the filament axis. Gravitational instability in the filaments initiated cloud fragmentation that hierarchically led to core collapse to form the protostars, as demonstrated by the several dense cloud cores indeed detected along the filament axis. As seen in Figure 13(a), the gas velocity is coherently high in the vicinity of BD+45 3216, and decreases gradually further away. Clearly the expanding H II region has excavated the nearby clouds. Toward Clump A, gravity accelerates the gas where higher excitation temperatures (~ 12 – 13 K) are detected at velocity < -4 km s $^{-1}$. The entire cloud therefore encapsulates a complex site hosting young stellar subgroups at various evolutionary stages, with entangled filaments and fragments undergoing cloud disruption.

6. SUMMARY AND CONCLUSIONS

We have diagnosed the stellar contents in the S112 complex using multiwavelength data. The interplay of

young stellar evolution, dust clouds, and ionized gas is established to scrutinize the overall star formation history in the region. The key results are summarized as follows:

1. The K -band extinction map in a $\sim 2^\circ$ region uncovers the filamentary structure of dust along the Galactic east-west extension. The overall extinction is moderate, averaging $A_V \sim 2.78$ mag, except a few clumps reaching maxima of $A_V \sim 17$ mag.
2. The complex harbours more than 500 young objects identified using infrared excess, which have the best isochrone-fitting age of ~ 1 Myr. Additionally, more than 350 H α emission-line stars are detected, standing out among even the most prominent star-forming regions, thereby signifying excessive ionization activity in the complex.
3. The spatial distribution of the YSOs shows a preferential alignment along the filamentary clouds, coinciding with the radio emissions, indicative of a star formation activity stretching an angular scale of $\sim 2^\circ$.
4. The molecular cloud traced by the CO gas has a median velocity of ~ -3.65 km s $^{-1}$, with a gradual increase from the Galactic east (~ -4 km s $^{-1}$) to west (~ -2.5 km s $^{-1}$). The filament, extending over ~ 80 pc, shows evidence of cloud fragmentation and formation of multiple compact and dense cloud cores that correlate with YSO groupings. Overall, the filament temperature remains coherent (~ 10 K), except near dense cores (column density $> 10^{22}$ cm $^{-2}$) where it reaches up to ~ 32 K.
5. The highest concentrations of YSOs are confined at three locations, referred to as Clump A, S112, and Clump B, all interconnected via cloud filaments, with a “filament-hub” configuration that supports the notion of mass channeling through filaments in radiant morphology to feed the massive stars or star clusters as hubs.
6. Analysis of the ionized gas associated with S112 and Clump B using radio continuum observations leads to an estimate of their dynamical ages being ~ 0.18 – 1.0 Myr, consistent with the age estimation from the isochrone fitting of the young stars.
7. Spectroscopy of luminous stars suggests the O8 V star BD+45 3216 to be the only viable ionizing source in the region. Its location relative to

the young population, ionized gas, and molecular cloud suggests a triggering star formation sequence in the blister-shaped S112 H II region.

ACKNOWLEDGEMENTS

AP acknowledges the support by S. N. Bose National Centre for Basic Sciences, funded by the Department of Science and Technology, India. We are thankful to the staff of the Indian Astronomical Observatory, Hanle and Centre for Research and Education in Science & Technology, Hosakote for their assistance during observations at HCT, operated by the Indian Institute of Astrophysics, Bangalore. This work has made use of data from the European Space Agency (ESA) mission *Gaia* (<https://www.cosmos.esa.int/gaia>), processed by the *Gaia* Data Processing and Analysis Consortium (DPAC, <https://www.cosmos.esa.int/web/gaia/dpac/consortium>). This work makes use of data obtained as part of the IPHAS carried out at the INT, operated by the Isaac Newton Group. Data products from the 2MASS, which is a joint project of the Uni-

versity of Massachusetts and the IPAC/Caltech are employed. This publication has made use of data products from the WISE, which is a joint project of the University of California, Los Angeles, and the Jet Propulsion Laboratory/Caltech, funded by the National Aeronautics and Space Administration. Part of this research is based on observations with AKARI, a Japan Aerospace Exploration Agency project with the participation of ESA. Radio images are obtained from the NVSS archive, observed by the NRAO, a facility of the National Science Foundation operated under cooperative agreement by Associated Universities, Inc. This work also uses observations made with the Planck mission, which is a project of the ESA with contributions provided by ESA member states. We are thankful to the referee for an insightful review that largely improved the scientific content of the paper.

Software: IRAF (Tody 1986), GILDAS (Gildas Team 2013), Astropy Project (Astropy Collaboration et al. 2018), APLpy (Robitaille 2019)

REFERENCES

- Alexander, M. J., Kobulnicky, H. A., Kerton, C. R., & Arvidsson, K. 2013, *ApJ*, 770, 1, doi: [10.1088/0004-637X/770/1/1](https://doi.org/10.1088/0004-637X/770/1/1)
- Anderson, L. D., Armentrout, W. P., Johnstone, B. M., et al. 2015, *ApJS*, 221, 26, doi: [10.1088/0067-0049/221/2/26](https://doi.org/10.1088/0067-0049/221/2/26)
- André, P., Revéret, V., Könyves, V., et al. 2016, *A&A*, 592, A54, doi: [10.1051/0004-6361/201628378](https://doi.org/10.1051/0004-6361/201628378)
- Astropy Collaboration, Price-Whelan, A. M., Sipőcz, B. M., et al. 2018, *AJ*, 156, 123, doi: [10.3847/1538-3881/aabc4f](https://doi.org/10.3847/1538-3881/aabc4f)
- Bailer-Jones, C. A. L., Rybizki, J., Fouesneau, M., Demleitner, M., & Andrae, R. 2021, *AJ*, 161, 147, doi: [10.3847/1538-3881/abd806](https://doi.org/10.3847/1538-3881/abd806)
- Bailer-Jones, C. A. L., Rybizki, J., Fouesneau, M., Mantelet, G., & Andrae, R. 2018, *AJ*, 156, 58, doi: [10.3847/1538-3881/aacb21](https://doi.org/10.3847/1538-3881/aacb21)
- Barentsen, G., Farnhill, H. J., Drew, J. E., et al. 2014, *MNRAS*, 444, 3230, doi: [10.1093/mnras/stu1651](https://doi.org/10.1093/mnras/stu1651)
- Bessell, M. S., & Brett, J. M. 1988, *PASP*, 100, 1134, doi: [10.1086/132281](https://doi.org/10.1086/132281)
- Bisbas, T. G., Wünsch, R., Whitworth, A. P., & Hubber, D. A. 2009, *A&A*, 497, 649, doi: [10.1051/0004-6361/200811522](https://doi.org/10.1051/0004-6361/200811522)
- Blitz, L., Fich, M., & Stark, A. A. 1982, *ApJS*, 49, 183, doi: [10.1086/190795](https://doi.org/10.1086/190795)
- Bolatto, A. D., Wolfire, M., & Leroy, A. K. 2013, *ARA&A*, 51, 207, doi: [10.1146/annurev-astro-082812-140944](https://doi.org/10.1146/annurev-astro-082812-140944)
- Bressan, A., Marigo, P., Girardi, L., et al. 2012, *MNRAS*, 427, 127, doi: [10.1111/j.1365-2966.2012.21948.x](https://doi.org/10.1111/j.1365-2966.2012.21948.x)
- Clark, P. C., & Glover, S. C. O. 2014, *MNRAS*, 444, 2396, doi: [10.1093/mnras/stu1589](https://doi.org/10.1093/mnras/stu1589)
- Cohen, J. G., Frogel, J. A., Persson, S. E., & Elias, J. H. 1981, *ApJ*, 249, 481, doi: [10.1086/159308](https://doi.org/10.1086/159308)
- Condon, J. J., Cotton, W. D., Greisen, E. W., et al. 1998, *AJ*, 115, 1693, doi: [10.1086/300337](https://doi.org/10.1086/300337)
- Danks, A. C., & Dennefeld, M. 1994, *PASP*, 106, 382, doi: [10.1086/133390](https://doi.org/10.1086/133390)
- Das, S. R., Jose, J., Samal, M. R., Zhang, S., & Panwar, N. 2021, *MNRAS*, 500, 3123, doi: [10.1093/mnras/staa3222](https://doi.org/10.1093/mnras/staa3222)
- Deharveng, L., Zavagno, A., & Caplan, J. 2005, *A&A*, 433, 565, doi: [10.1051/0004-6361:20041946](https://doi.org/10.1051/0004-6361:20041946)
- Dobashi, K., Bernard, J.-P., Yonekura, Y., & Fukui, Y. 1994, *ApJS*, 95, 419, doi: [10.1086/192106](https://doi.org/10.1086/192106)
- Doi, Y., Takita, S., Ootsubo, T., et al. 2015, *PASJ*, 67, 50, doi: [10.1093/pasj/psv022](https://doi.org/10.1093/pasj/psv022)
- Drew, J. E., Greimel, R., Irwin, M. J., et al. 2005, *MNRAS*, 362, 753, doi: [10.1111/j.1365-2966.2005.09330.x](https://doi.org/10.1111/j.1365-2966.2005.09330.x)
- Dyson, J. E., & Williams, D. A. 1980, *Physics of the interstellar medium*
- Egan, M. P., Price, S. D., Kraemer, K. E., et al. 2003, *VizieR Online Data Catalog*, V/114
- Elias, J. H., Frogel, J. A., Matthews, K., & Neugebauer, G. 1982, *AJ*, 87, 1029, doi: [10.1086/113185](https://doi.org/10.1086/113185)

- Elmegreen, B. G. 1993, in *Protostars and Planets III*, ed. E. H. Levy & J. I. Lunine, 97
- Elmegreen, B. G. 1998, in *Astronomical Society of the Pacific Conference Series*, Vol. 148, *Origins*, ed. C. E. Woodward, J. M. Shull, & J. Thronson, Harley A., 150. <https://arxiv.org/abs/astro-ph/9712352>
- Elmegreen, B. G., & Lada, C. J. 1977, *ApJ*, 214, 725, doi: [10.1086/155302](https://doi.org/10.1086/155302)
- Esimbek, J., Wu, Y., & Wang, Y. 2008, *NewA*, 13, 144, doi: [10.1016/j.newast.2007.08.002](https://doi.org/10.1016/j.newast.2007.08.002)
- Evans, D. W., Riello, M., De Angeli, F., et al. 2018, *A&A*, 616, A4, doi: [10.1051/0004-6361/201832756](https://doi.org/10.1051/0004-6361/201832756)
- Evans, N. J., I., & Lada, E. A. 1991, in *Fragmentation of Molecular Clouds and Star Formation*, ed. E. Falgarone, F. Boulanger, & G. Duvert, Vol. 147, 293
- Falgarone, E., Phillips, T. G., & Walker, C. K. 1991, *ApJ*, 378, 186, doi: [10.1086/170419](https://doi.org/10.1086/170419)
- Fazio, G. G., Hora, J. L., Allen, L. E., et al. 2004, *ApJS*, 154, 10, doi: [10.1086/422843](https://doi.org/10.1086/422843)
- Flaherty, K. M., Pipher, J. L., Megeath, S. T., et al. 2007, *ApJ*, 663, 1069, doi: [10.1086/518411](https://doi.org/10.1086/518411)
- Fukuda, N., & Hanawa, T. 2000, *ApJ*, 533, 911, doi: [10.1086/308701](https://doi.org/10.1086/308701)
- Gaia Collaboration, Brown, A. G. A., Vallenari, A., et al. 2018, *A&A*, 616, A1, doi: [10.1051/0004-6361/201833051](https://doi.org/10.1051/0004-6361/201833051)
- . 2021, *A&A*, 649, A1, doi: [10.1051/0004-6361/202039657](https://doi.org/10.1051/0004-6361/202039657)
- Garay, G., & Rodriguez, L. F. 1983, *ApJ*, 266, 263, doi: [10.1086/160775](https://doi.org/10.1086/160775)
- Gildas Team. 2013, *GILDAS: Grenoble Image and Line Data Analysis Software*. <http://ascl.net/1305.010>
- Gutermuth, R. A., Megeath, S. T., Myers, P. C., et al. 2009, *ApJS*, 184, 18, doi: [10.1088/0067-0049/184/1/18](https://doi.org/10.1088/0067-0049/184/1/18)
- Gutermuth, R. A., Megeath, S. T., Pipher, J. L., et al. 2005, *ApJ*, 632, 397, doi: [10.1086/432460](https://doi.org/10.1086/432460)
- Hernández, J., Calvet, N., Briceño, C., Hartmann, L., & Berlind, P. 2004, *AJ*, 127, 1682, doi: [10.1086/381908](https://doi.org/10.1086/381908)
- Hunter, D. A., & Massey, P. 1990, *AJ*, 99, 846, doi: [10.1086/115378](https://doi.org/10.1086/115378)
- Israel, F. P. 1978, *A&A*, 70, 769
- Ivanov, V. D., Borissova, J., Bresolin, F., & Pessev, P. 2005, *A&A*, 435, 107, doi: [10.1051/0004-6361:20042337](https://doi.org/10.1051/0004-6361:20042337)
- Jacoby, G. H., Hunter, D. A., & Christian, C. A. 1984, *ApJS*, 56, 257, doi: [10.1086/190983](https://doi.org/10.1086/190983)
- Kauffmann, J., Pillai, T., & Goldsmith, P. F. 2013, *ApJ*, 779, 185, doi: [10.1088/0004-637X/779/2/185](https://doi.org/10.1088/0004-637X/779/2/185)
- Kobulnicky, H. A., Lundquist, M. J., Bhattacharjee, A., & Kerton, C. R. 2012, *AJ*, 143, 71, doi: [10.1088/0004-6256/143/3/71](https://doi.org/10.1088/0004-6256/143/3/71)
- Koenig, X. P., Leisawitz, D. T., Benford, D. J., et al. 2012, *ApJ*, 744, 130, doi: [10.1088/0004-637X/744/2/130](https://doi.org/10.1088/0004-637X/744/2/130)
- Kumar, M. S. N., Arzoumanian, D., Men'shchikov, A., et al. 2022, *A&A*, 658, A114, doi: [10.1051/0004-6361/202140363](https://doi.org/10.1051/0004-6361/202140363)
- Kwan, J. 1997, *ApJ*, 489, 284, doi: [10.1086/304773](https://doi.org/10.1086/304773)
- Lada, C. J., Lada, E. A., Clemens, D. P., & Bally, J. 1994, *ApJ*, 429, 694, doi: [10.1086/174354](https://doi.org/10.1086/174354)
- Lahulla, J. F. 1985, *A&AS*, 61, 537
- Lawrence, A., Warren, S. J., Almaini, O., et al. 2007, *MNRAS*, 379, 1599, doi: [10.1111/j.1365-2966.2007.12040.x](https://doi.org/10.1111/j.1365-2966.2007.12040.x)
- Lucas, P. W., Hoare, M. G., Longmore, A., et al. 2008, *MNRAS*, 391, 136, doi: [10.1111/j.1365-2966.2008.13924.x](https://doi.org/10.1111/j.1365-2966.2008.13924.x)
- Martín-Hernández, N. L., van der Hulst, J. M., & Tielens, A. G. G. M. 2003, *A&A*, 407, 957, doi: [10.1051/0004-6361:20030982](https://doi.org/10.1051/0004-6361:20030982)
- Martins, F., & Plez, B. 2006, *A&A*, 457, 637, doi: [10.1051/0004-6361:20065753](https://doi.org/10.1051/0004-6361:20065753)
- Matsakis, D. N., Evans, N. J., I., Sato, T., & Zuckerman, B. 1976, *AJ*, 81, 172, doi: [10.1086/111871](https://doi.org/10.1086/111871)
- Maud, L. T., Moore, T. J. T., Lumsden, S. L., et al. 2015, *MNRAS*, 453, 645, doi: [10.1093/mnras/stv1635](https://doi.org/10.1093/mnras/stv1635)
- Meyer, M. R., Calvet, N., & Hillenbrand, L. A. 1997, *AJ*, 114, 288, doi: [10.1086/118474](https://doi.org/10.1086/118474)
- Murakami, H., Baba, H., Barthel, P., et al. 2007, *PASJ*, 59, S369, doi: [10.1093/pasj/59.sp2.S369](https://doi.org/10.1093/pasj/59.sp2.S369)
- Myers, P. C. 2009, *ApJ*, 700, 1609, doi: [10.1088/0004-637X/700/2/1609](https://doi.org/10.1088/0004-637X/700/2/1609)
- Neugebauer, G., Habing, H. J., van Duinen, R., et al. 1984, *ApJL*, 278, L1, doi: [10.1086/184209](https://doi.org/10.1086/184209)
- Ojha, D. K., Samal, M. R., Pandey, A. K., et al. 2011, *ApJ*, 738, 156, doi: [10.1088/0004-637X/738/2/156](https://doi.org/10.1088/0004-637X/738/2/156)
- Oke, J. B. 1990, *AJ*, 99, 1621, doi: [10.1086/115444](https://doi.org/10.1086/115444)
- Panagia, N. 1973, *AJ*, 78, 929, doi: [10.1086/111498](https://doi.org/10.1086/111498)
- Panja, A., Chen, W. P., Dutta, S., et al. 2021, *ApJ*, 910, 80, doi: [10.3847/1538-4357/abded4](https://doi.org/10.3847/1538-4357/abded4)
- Panja, A., Mondal, S., Dutta, S., et al. 2020, *AJ*, 159, 153, doi: [10.3847/1538-3881/ab737a](https://doi.org/10.3847/1538-3881/ab737a)
- Panwar, N., Sharma, S., Ojha, D. K., et al. 2020, *ApJ*, 905, 61, doi: [10.3847/1538-4357/abc42e](https://doi.org/10.3847/1538-4357/abc42e)
- Pecaut, M. J., & Mamajek, E. E. 2013, *ApJS*, 208, 9, doi: [10.1088/0067-0049/208/1/9](https://doi.org/10.1088/0067-0049/208/1/9)
- Planck Collaboration, Ade, P. A. R., Aghanim, N., et al. 2016, *A&A*, 594, A28, doi: [10.1051/0004-6361/201525819](https://doi.org/10.1051/0004-6361/201525819)
- Reid, M. J., Menten, K. M., Brunthaler, A., et al. 2019, *ApJ*, 885, 131, doi: [10.3847/1538-4357/ab4a11](https://doi.org/10.3847/1538-4357/ab4a11)
- Robitaille, T. 2019, *APLpy v2.0: The Astronomical Plotting Library in Python, 2.0*, Zenodo, doi: [10.5281/zenodo.2567476](https://doi.org/10.5281/zenodo.2567476)
- Singh, A., Matzner, C. D., Friesen, R. K., et al. 2021, *ApJ*, 922, 87, doi: [10.3847/1538-4357/ac20d2](https://doi.org/10.3847/1538-4357/ac20d2)

- Skrutskie, M. F., Cutri, R. M., Stiening, R., et al. 2006, AJ, 131, 1163, doi: [10.1086/498708](https://doi.org/10.1086/498708)
- Su, Y., Yang, J., Zhang, S., et al. 2019, ApJS, 240, 9, doi: [10.3847/1538-4365/aaf1c8](https://doi.org/10.3847/1538-4365/aaf1c8)
- Sun, Y., Yang, J., Xu, Y., et al. 2020, ApJS, 246, 7, doi: [10.3847/1538-4365/ab5b97](https://doi.org/10.3847/1538-4365/ab5b97)
- Sun, Y., Yang, J., Yan, Q.-Z., et al. 2021, ApJS, 256, 32, doi: [10.3847/1538-4365/ac11fe](https://doi.org/10.3847/1538-4365/ac11fe)
- Tody, D. 1986, in Society of Photo-Optical Instrumentation Engineers (SPIE) Conference Series, Vol. 627, Instrumentation in astronomy VI, ed. D. L. Crawford, 733, doi: [10.1117/12.968154](https://doi.org/10.1117/12.968154)
- Torres-Dodgen, A. V., & Weaver, W. B. 1993, PASP, 105, 693, doi: [10.1086/133222](https://doi.org/10.1086/133222)
- Urquhart, J. S., Hoare, M. G., Purcell, C. R., et al. 2009, A&A, 501, 539, doi: [10.1051/0004-6361/200912108](https://doi.org/10.1051/0004-6361/200912108)
- Walborn, N. R., & Fitzpatrick, E. L. 1990, PASP, 102, 379, doi: [10.1086/132646](https://doi.org/10.1086/132646)
- Wright, E. L., Eisenhardt, P. R. M., Mainzer, A. K., et al. 2010, AJ, 140, 1868, doi: [10.1088/0004-6256/140/6/1868](https://doi.org/10.1088/0004-6256/140/6/1868)